

Spatiotemporal dynamics of membrane surface charge regulates cell polarity and migration

Received: 4 November 2021

Accepted: 18 August 2022

Published online: 6 October 2022

 Check for updates

Tatsat Banerjee ^{1,2}, Debojyoti Biswas^{3,5}, Dhiman Sankar Pal ^{1,5},
Yuchuan Miao ^{1,4}, Pablo A. Iglesias ^{1,3} and Peter N. Devreotes ^{1,4} 

During cell migration and polarization, numerous signal transduction and cytoskeletal components self-organize to generate localized protrusions. Although biochemical and genetic analyses have delineated many specific interactions, how the activation and localization of so many different molecules are spatiotemporally orchestrated at the subcellular level has remained unclear. Here we show that the regulation of negative surface charge on the inner leaflet of the plasma membrane plays an integrative role in the molecular interactions. Surface charge, or zeta potential, is transiently lowered at new protrusions and within cortical waves of Ras/PI3K/TORC2/F-actin network activation. Rapid alterations of inner leaflet anionic phospholipids—such as PI(4,5)P₂, PI(3,4)P₂, phosphatidylserine and phosphatidic acid—collectively contribute to the surface charge changes. Abruptly reducing the surface charge by recruiting positively charged optogenetic actuators was sufficient to trigger the entire biochemical network, initiate *de novo* protrusions and abrogate pre-existing polarity. These effects were blocked by genetic or pharmacological inhibition of key signalling components such as AKT and PI3K/TORC2. Conversely, increasing the negative surface charge deactivated the network and locally suppressed chemoattractant-induced protrusions or subverted EGF-induced ERK activation. Computational simulations involving excitable biochemical networks demonstrated that slight changes in feedback loops, induced by recruitment of the charged actuators, could lead to outsized effects on system activation. We propose that key signalling network components act on, and are in turn acted upon, by surface charge, closing feedback loops, which bring about the global-scale molecular self-organization required for spontaneous protrusion formation, cell migration and polarity establishment.

Cell migration and polarity involve large networks of interacting signal transduction and cytoskeletal components^{1–4}. The spatial and temporal behaviour of the molecular events are highly coordinated—for example, Ras, PI3K and Rac activation along with actin polymerization

define growing protrusions, while PTEN, RhoA and myosin II leave these regions and return to the membrane only when the protrusions are withdrawn. Where it has been examined, this complementary organization is conserved during macropinocytosis, phagocytosis and cytokinesis as

A full list of affiliations appears at the end of the paper. ✉ e-mail: pnd@jhmi.edu

well as within travelling cortical waves in different cells throughout phylogeny and in apical–basal polarity of epithelial cells^{5–7}. Furthermore, genetic, pharmacological or mechanical perturbations of different individual components often result in similar phenotypic changes, suggesting that the overall ‘setpoint’ of the network is more important than any single constituent^{8–18}. Although these emergent features could be a result of a series of stepwise protein–protein/protein–lipid interactions, it seems more probable that they are linked to some organizing principle, such as a biophysical property of the plasma membrane¹⁹. Such global organizers have been suggested^{1,10,19} but properties that track closely with the observed spatial and temporal organization or whose small alterations bring about large shifts in network behaviour have not been identified.

One candidate for such a biophysical organizer is the surface charge, or zeta potential, of the inner membrane. Cells maintain a negative charge on the inner leaflet of the plasma membrane, primarily by regulating the concentrations of multiple anionic phospholipids^{20–23}. Numerous studies have focused on the signalling properties of individual lipids such as PIP3 (refs. 24,25). Many cytoskeletal proteins have been reported to bear PI(4,5)P2-binding motifs²⁶. However, relatively few studies have focused on the role of surface charge itself^{20,27}. These have proposed that the zeta potential, from –20 to –50 mV (refs. 27–29), regulates local pH and second messenger concentrations, alters ion channel conductance and controls peripheral membrane protein association^{20–23,30–33}. Moreover, during immunological synapse and phagocytosis, the surface charge of the plasma membrane changes^{21,34–36}. However, whether signalling/cytoskeletal network activation is associated with increases or decreases in the surface charge or whether direct perturbations of the surface charge can activate/deactivate the networks has not been explored. Interestingly, it has been reported that enzymatic lowering of specific anionic lipids such as PI(4,5)P2 and PI(3,4)P2, which would be expected to decrease the surface charge, can lead to network activation and enhanced cell migration^{9,37}.

To assess the possible role of membrane surface charge as a biophysical organizer, we examined changes in the surface charge profile during cell migration and polarity, and designed actuators to directly alter the charge. We discovered that PI(4,5)P2, PI(3,4)P2, phosphatidylserine (PS) and phosphatidic acid (PA) are dynamically lowered in local regions of the membrane where the Ras/PI3K/AKT/F-actin network is activated. Consistent with these data, we observed that the overall surface potential is high in resting membranes and transiently lowered during network activation and protrusion formation. By recruiting positively or negatively charged optogenetic actuators to the membrane in a spatiotemporally controlled fashion, we established that the level of surface potential in local membrane domains is sufficient and necessary to control the activation of the entire signal transduction network and to direct migration and polarity phenotypes.

Results

To analyse the coordinated signalling and cytoskeletal activities, we examined protrusions in migrating *Dictyostelium* cells as well as cortical waves in *Dictyostelium* cells and RAW 264.7 macrophages (Extended Data Fig. 1a–c). As previously noted^{5,25,38}, events that facilitate protrusion formation, such as Ras/PI3K activation and actin polymerization, localize to the front regions of migrating cells (Extended Data Fig. 1a,d), whereas those that suppress protrusions, such as PTEN and myosin II, localize to the back regions (Extended Data Fig. 1e). A corresponding complementarity was observed in ventral wave patterns where the molecules/events dynamically separate into broad propagating ‘front-state’ and ‘back-state’ regions (Extended Data Fig. 1f–i)^{6,39–41}. Wave properties have been previously shown to control modes of protrusions and cell migration and thus serve as a useful surrogate for front/back polarity (Extended Data Fig. 1i). To quantitate the extent to which an event/component was co-localized or complementarily localized with the front marker PIP3, we developed a conditional probability (CP)-based index (Methods and Extended Data Fig. 2a–d). For most of the data, we have provided both normalized line scans and CP indices to report measures of fractional changes in sensor levels and the extent of complementarity with respect to PIP3.

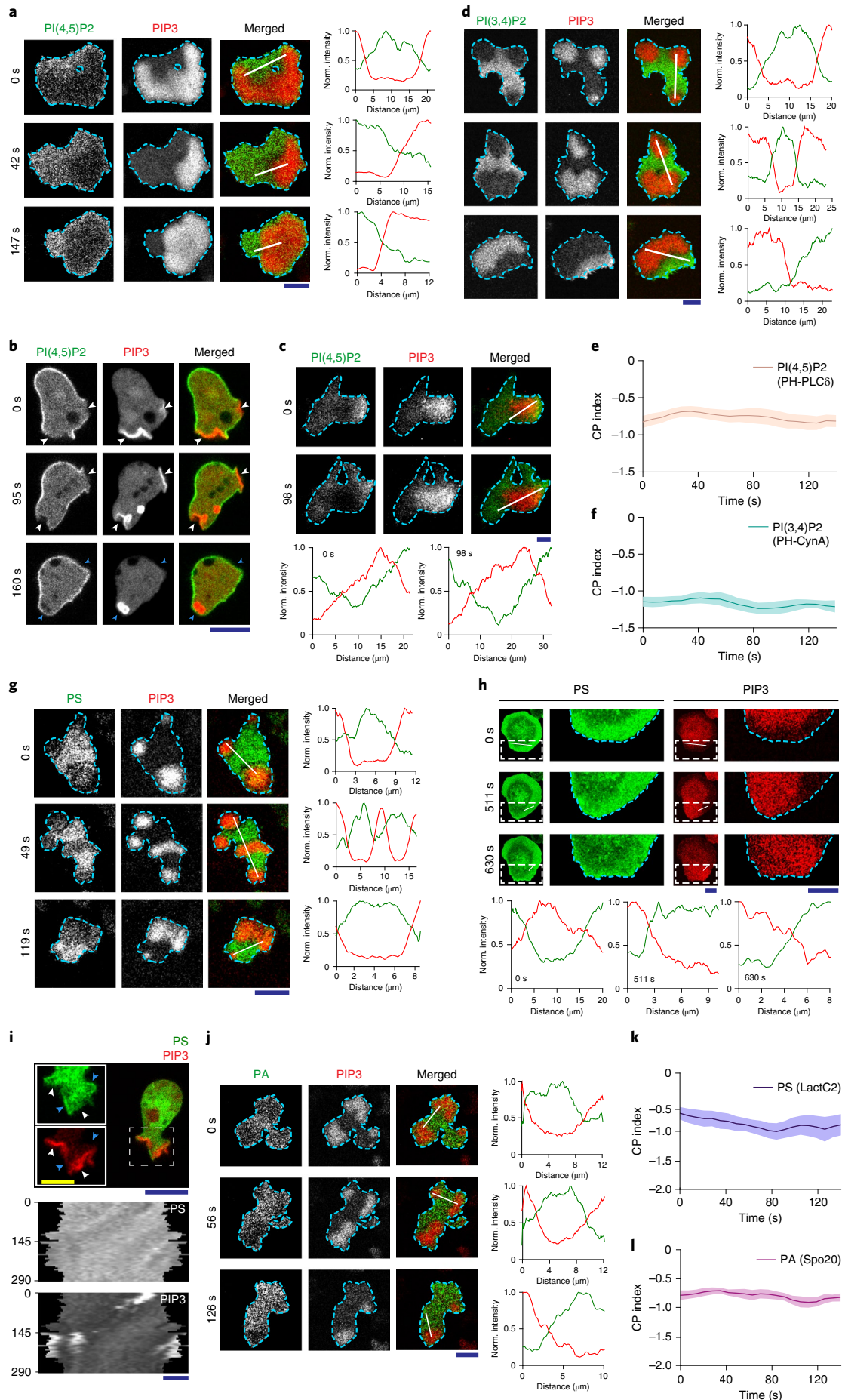
PI(4,5)P2, PI(3,4)P2, PS and PA localize to the back-state regions of the membrane

Using genetically encoded biosensors, we discovered that several anionic phospholipids display similar dynamic patterns on the inner membrane. The distribution of the biosensor PH_{PLC6} indicated that PI(4,5)P2 was depleted in the front-state regions of ventral waves and from protrusions in migrating *Dictyostelium* cells (Fig. 1a,b and Supplementary Video 1). Equivalent patterns of PI(4,5)P2 were observed in the ventral waves of RAW 264.7 macrophages (Fig. 1c, Extended Data Fig. 3a and Supplementary Video 1), as previously reported^{42,43}. The PI(3,4)P2 biosensor PH_{Cyna} displayed a similar pattern in the *Dictyostelium* ventral waves (Fig. 1d, Extended Data Fig. 3b and Supplementary Video 2), consistent with our previous reports of its depletion from the protrusions^{37,44}. Line scans showed 40–70% less PI(4,5)P2 and PI(3,4)P2 in the front regions compared with the back regions of the waves. The consistently high negative CP index values for PI(4,5)P2 and PI(3,4)P2 showed that the complementarity with respect to PIP3 was maintained as the waves propagated (Figs. 1e,f).

Given that these two signalling lipids co-segregated to the back state of the membrane, we investigated whether other major anionic phospholipids exhibit asymmetrical patterns. Using the biosensor LactC2, we found that PS, which accounts for approximately 20% of inner-leaflet lipids^{45,46}, also localized to the back states of the ventral waves of *Dictyostelium* cells (Fig. 1g, Extended Data Fig. 3c and Supplementary Video 3) and RAW 264.7 macrophages (Fig. 1h, Extended

Fig. 1 | Multiple anionic phospholipids dynamically self-organize to the back-state regions of the membrane. **a, b**, Representative live-cell time-lapse images of *Dictyostelium* cells coexpressing the PI(4,5)P2 sensor PH_{PLC6}-GFP and PI(3,4,5)P3 sensor PH_{Crac}-mCherry during ventral wave propagation (**a**) and migration (**b**) showing PH_{PLC6} dynamically localizes to the back-state regions in ventral waves (**a**) and analogously moves away from protrusions in migrating cells (**b**). **b**, The white arrowheads point to protrusions where PIP3 is enriched and PI(4,5)P2 is depleted; the blue arrowheads indicate PH_{PLC6} returning to the membrane domains where protrusions were retracted. **c**, Live-cell images of a RAW 264.7 macrophage coexpressing PH_{PLC6}-GFP and PH_{AKT}-mCherry demonstrating dynamic complimentary distribution in its ventral waves. **d**, Live-cell images of *Dictyostelium* cells coexpressing PH_{Crac}-mCherry and the PI(3,4)P2 sensor PH_{Cyna}-KikGR demonstrating the spatiotemporal back localization of PI(3,4)P2 in its ventral waves. **e, f**, Time-series plots of the CP index for PI(4,5)P2 (**e**; $n_c = 16$ cells) and PI(3,4)P2 (**f**; $n_c = 11$ cells). **g, h**, Dynamic back-state distribution of the PS biosensor GFP-LactC2 in the ventral waves of *Dictyostelium* cells (**g**) and in RAW 264.7 macrophages (**h**). Front-state regions

are marked by PIP3 sensor PH_{Crac}-mCherry (**g**) or PH_{AKT}-mCherry (**h**). Magnified views of the region enclosed in the dashed white boxes are shown to the right (**h**). **i**, Analogous depletion of GFP-LactC2 from protrusions in migrating *Dictyostelium* cells. Protrusions are marked by PIP3. Live-cell image (top) and 360° membrane kymographs around the cell perimeter (middle and bottom) are shown. In the top panel inset, blue arrowheads show PS-rich membrane regions and white arrowheads show PIP3-rich membrane regions. In both kymographs, the numbers on the left denote time in seconds. **j**, Complementary localization of the PA sensor GFP-Spo20 and PIP3 in *Dictyostelium* ventral waves. **k, l**, Extent of back localization of PS and PA shown in terms of time-series plots of the CP index of LactC2 (**k**; $n_c = 15$ cells) and Spo20 (**l**; $n_c = 16$ cells), respectively. **a, c, d, g, h, j**, Line scans along the solid white lines are shown on the right (**a, d, g, j**) or bottom (**c, h**). Dashed blue lines indicate cell boundary. Norm., normalized. **e, f, k, l**, Each of the n_c cells was analysed for $n_t = 20$ frames; all CP indices were calculated with respect to PIP3; data are the mean \pm s.e.m. Scale bars, 5 μ m (yellow scale bar in **j**) and 10 μ m (blue scale bars). Source numerical data are provided.



Data Fig. 3d and Supplementary Video 3), and was depleted from protrusions in migrating *Dictyostelium* (Fig. 1i). Using the biosensor Spo20 (refs. 47,48), we observed that PA also preferentially distributed to the back-state regions of the ventral waves (Fig. 1j and Extended Data Fig. 3e) as well as away from protrusions (Extended Data Fig. 3f). Line scans showed 30–50% less PS and PA in the front regions of the waves relative to the back. The CP indices of PS and PA (Fig. 1k,l) were found to be consistently negative, similar to those of PI(4,5)P2, PI(3,4)P2 and PTEN (Extended Data Figs. 2d and 3g). Together, these observations show that four major anionic lipids decrease in the front-state regions of the membrane where PIP3 increases. Although PIP3 carries the most negative charge per molecule basis, it is a minor constituent^{45,49–51}.

Higher negative surface charge defines the back regions of the membrane

Reasoning that, with respect to charge, the decreases in the four predominant anionic phospholipids would more than offset increases in PIP3, we sought to measure the spatiotemporal changes in the inner-membrane surface charge. We used R(+8)-Pre, a charged prenylated peptide (Supplementary Table 1), which has been characterized in vitro to detect the combination of anionic lipids^{21,28,52}. Consistent with the four anionic lipid distributions, the back-state regions of cortical waves in *Dictyostelium* cells are defined by a higher negative surface charge compared with the front-state regions (Fig. 2a and Supplementary Video 4). Line scans demonstrated 30–60% less charge sensor in the front compared with the back regions of the waves (Fig. 2a). Despite continuous wave propagation, as marked by PIP3, the surface charge sensor maintained its back-state localization (Fig. 2b). Similarly, protrusions on migrating cells were depleted of R(+8)-Pre relative to the basal level on the membrane (Fig. 2c and Supplementary Video 4). An analogous spatiotemporal distribution of surface charge was also observed in the ventral waves of RAW 264.7 macrophages (Fig. 2d,e and Supplementary Video 5).

As previously reported for patterns of signalling events such as PIP3 accumulation and PTEN dissociation (Extended Data Fig. 1h)^{40,41,53}, we found that the dynamic distribution of surface charge was relatively independent of the actin cytoskeleton. In latrunculin A-treated *Dictyostelium* cells in which periodic circulating waves were induced, the charge sensor continuously adjusted its localization towards the back state (Fig. 2f,g). In agreement with this, as shown in Fig. 2h and Extended Data Fig. 4a, when latrunculin A-treated cells were exposed to a chemotactic gradient, R(+8)-Pre, like the standard back protein PTEN, moved away from the typical front-region crescent of PIP3

(refs. 54,55). In all these scenarios, the CP indices indicated that the extent of complementarity to PIP3 was comparable to that of the established back protein PTEN (Fig. 2i and Extended Data Fig. 2d).

These asymmetrical distributions depended on charge and not on the specific amino-acid sequences of the sensor. As the positively charged arginines of the sensor were sequentially replaced with neutral glutamines (Supplementary Table 1), the distribution became increasingly uniform (Fig. 2j–l and Extended Data Fig. 4b–f). The dynamics of R(+2)-Pre (Fig. 2j,k and Extended Data Figs. 4d,f) resembled the uniform distribution of the G-protein-coupled receptor (GPCR) cAR1 (Extended Data Fig. 4g,h), the weakly charged myristoylated sequence of LYN (Extended Data Fig. 4i) and the uncharged prenylated carboxy (C)-terminal tail of HRas (Fig. 2m and Extended Data Fig. 4j), as quantified by CP indices (Fig. 2l,n,o). In contrast, two distinct polybasic sequences, PTEN_{1–18}-CAAX and RacG_{CT} (Supplementary Table 1)–carrying +6 and +7 charges, respectively—displayed a complementarity to PIP3 in the ventral waves and protrusions, which was roughly correlated with their net charge (Extended Data Fig. 5a–g). Thus, in the protrusions of migrating cells, activated crescents of latrunculin A-treated cells and activated regions of propagating waves, the front state of the membrane maintains a lower negative surface charge compared with the back state (Fig. 2p).

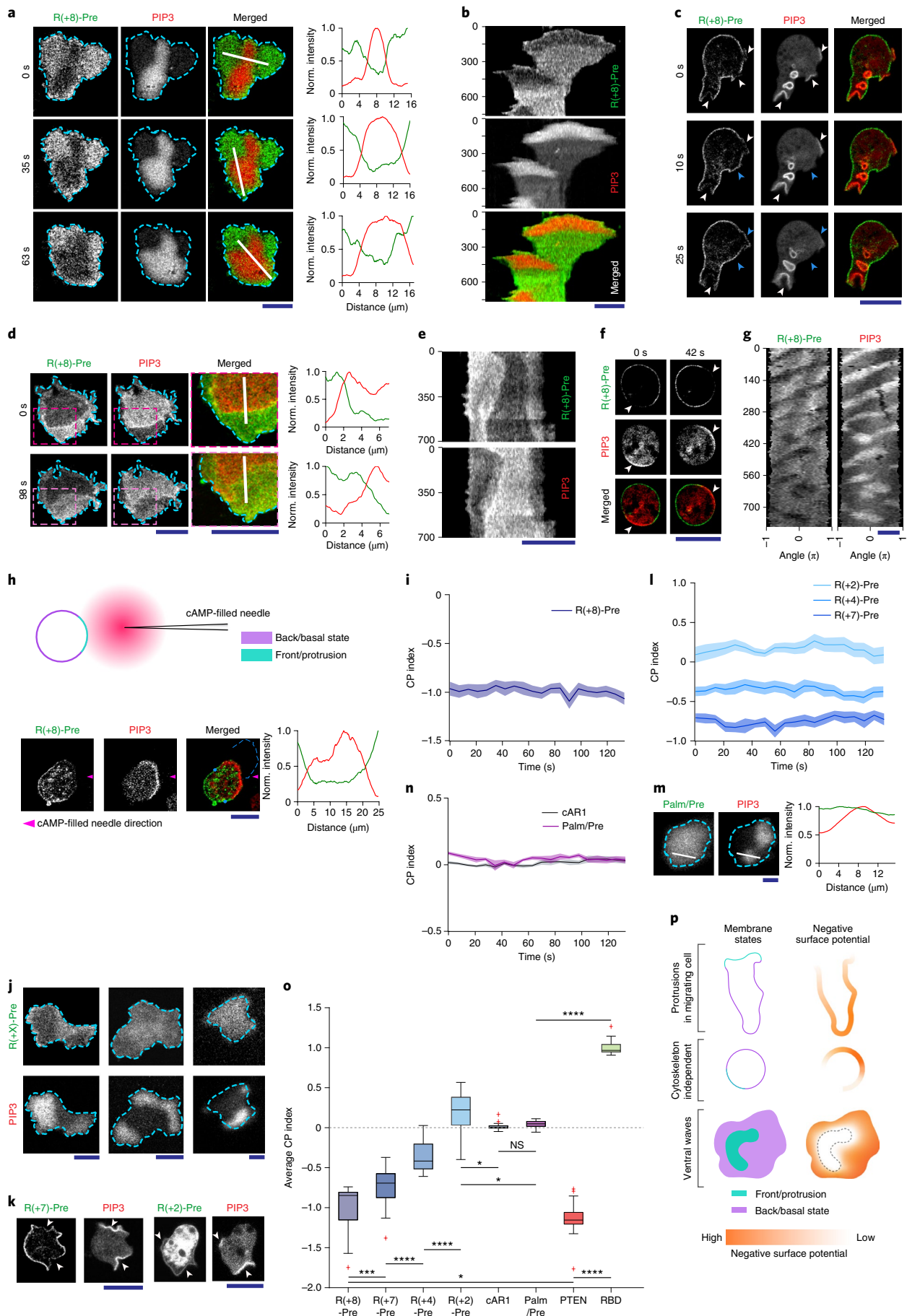
Anionic lipids contribute to surface charge in an integrative manner

Neither PI(4,5)P2 nor PI(3,4)P2 fully accounted for the asymmetrical distribution of the charge sensor. When we depleted PI(4,5)P2 by recruiting Inp54p to the membrane, PH_{PLC6} moved to the cytosol (Fig. 3a and Extended Data Fig. 6a), as expected. However, R(+8)-Pre remained membrane-bound (Figs. 3b,c). As previously published^{9,56}, cells with low PI(4,5)P2 levels displayed altered migration (Fig. 3d and Extended Data Fig. 6b,c) and expanded front regions. Importantly, R(+8)-Pre remained confined to diminished yet dynamically changing back regions (Fig. 3e). Similarly, in *Dd5p4* *Dictyostelium* cells, where PI(3,4)P2 levels are low³⁷, R(+8)-Pre stayed on the membrane (Extended Data Fig. 6d,e), marking the smaller but moving back-state regions (Fig. 3f). The membrane retention of R(+8)-Pre following Inp54p recruitment was not due to its binding to the product PI4P given that recruitment of pseudojanin—which simultaneously converts PI(4,5)P2 to PI4P and PI4P to PI⁵⁷—caused sensors for both PI(4,5)P2 (Fig. 3g and Supplementary Video 6) and PI4P (Fig. 3h and Supplementary Video 6) to move to the cytosol, but R(+8)-Pre largely remained on the membrane (Fig. 3i,j and Supplementary Video 7). Thus, dynamic regulation of the surface

Fig. 2 | The back state regions of the membrane maintains a higher negative surface charge on the inner leaflet compared to the front state regions.

a, Representative live-cell images of propagating ventral waves in a *Dictyostelium* cell coexpressing GFP-R(+8)-Pre (surface-charge sensor) and PH_{crac}-mCherry. **b**, Representative line kymographs of the wave patterns shown for the cells in **a**. **c**, Live-cell images of a migrating *Dictyostelium* cell showing that GFP-R(+8)-Pre is depleted in protrusions. The white arrowheads point to PIP3-enriched protrusions and the blue arrowheads to retracted protrusions. **d**, Ventral waves in RAW 264.7 macrophages coexpressing GFP-R(+8)-Pre and PH_{ACT}-mCherry displaying analogous complementary patterns. Magnified views of the regions of the red and pink boxes are provided (right). **e**, Representative line kymographs of the wave patterns shown for the cells in **d**. **f,g**, Live-cell images (**f**) and 360° membrane kymographs (**g**) of *Dictyostelium* cells coexpressing GFP-R(+8)-Pre and PH_{crac}-mCherry treated with the actin-polymerization inhibitor latrunculin A. **f**, The white arrowheads point to the front state, showing bright PIP3 patches and depletion of surface-charge sensor. **h**, R(+8)-Pre showing complementary localization with respect to the front-state marker PIP3 during chemotactic gradient stimulation-mediated receptor activation. The line scan along the dashed blue line is shown in the right panel (blue dots show the end points of the blue lines on the cell membrane). The cell was pretreated with Latrunculin A. **i**, Time-series plot of the CP index of R(+8)-Pre; $n_c = 29$ cells. **j**, Representative live-cell images of ventral waves of *Dictyostelium* cells coexpressing PH_{crac}-mCherry

as well as GFP-R(+7)-Pre (left), GFP-R(+4)-Pre (middle) or GFP-R(+2)-Pre (right). **k**, Live-cell images showing R(+7)-Pre and R(+2)-Pre distribution with respect to PIP3-rich protrusions (indicated by white arrowheads) in migrating cells. **l**, Time-series plot of CP indices of the mutated surface charge sensors R(+7)-Pre ($n_c = 23$), R(+4)-Pre ($n_c = 20$) and R(+2)-Pre ($n_c = 12$ cells). **m**, GFP-Palm/Pre exhibited uniform distribution on the ventral surface, whereas PH_{crac}-mCherry was enriched in the front-state regions. **n**, Time-series plot of the CP indices of the uniform membrane markers cAR1 ($n_c = 20$) and Palm/Pre ($n_c = 11$). **o**, Time-averaged CP indices of surface-charge sensors, uniform membrane marker controls, standard back protein PTEN ($n_c = 17$) and front-sensor RBD ($n_c = 15$). To generate each data point in the boxplots, the CP index values of $n_t = 20$ frames were averaged for each cell. The box-and-whisker plots were graphed using Tukey's method. The dashed grey line indicates CP index value of 0. *P* values were determined using a Mann–Whitney–Wilcoxon test; NS, not significant ($P > 0.05$); * $P \leq 0.05$; *** $P \leq 0.001$ and **** $P \leq 0.0001$. **p**, Schematic of the distribution of the negative surface potential in the front and back states of the cell membrane during migration (top), cytoskeleton-independent symmetry breaking (middle) and ventral wave propagation (bottom). **a,d,j,m**, Dashed blue lines indicate cell boundary. **a,d,m**, Line scans of all ventral waves along solid white lines are shown on the right. Norm., normalized. **b,e,g**, The numbers on the left denote time in seconds. **i,l,n**, data are the mean \pm s.e.m. Scale bars, 10 μ m. Source numerical data are provided.



charge depends on PI(4,5)P2 and PI(3,4)P2 but there are additional key contributors (such as PS and PA).

We sought a possible mechanism for the decreases in PS inside the activated regions of the inner membrane as, unlike phosphoinositides, PS is not modified by kinase/phosphatases. Reversible non-apoptotic flipping of PS was reported in several physiological contexts such as cytosolic calcium release and immunological stimulation^{58,59}, although a connection with signalling and cytoskeleton networks has not been established^{21,45}. We performed a transient annexin V-binding assay to label outer-leaflet PS during protrusion formation. Remarkably, on the outer leaflet, PS strongly localized to the protrusions (Fig. 3k), closely opposing its back-state distribution on the inner leaflet (Fig. 1g–i). In quiescent cells where protrusions were absent, annexin V did not bind to the outer leaflet (Extended Data Fig. 6f). The Pearson's correlation coefficient (r) values between the front-state/protrusion marker LimE and annexin V were similarly positive to that of the two front-state markers PH_{crac} and RBD (Fig. 3l), whereas the r value for the complementary pair PH_{crac} and PTEN was negative (Fig. 3l). More studies will be required but our data suggest that inner-leaflet PS may transiently flip to the outer leaflet in the membrane domains where the networks are activated.

PI(3,4,5)P3 is present at negligible amounts in the membrane^{45,49–51} and theoretically it can perform its well-known signalling functions without substantially contributing to surface charge⁵⁰. Nevertheless, we directly tested the contribution of PIP3 to the surface charge profile. First, cells were treated with the PI3K inhibitor LY294002 (refs. 60–63), which resulted in a loss of PIP3 accumulation in the protrusions (Fig. 3m). However, the typical depletion of the surface charge sensor from the protrusions was largely unchanged (Fig. 3m). Second, in *Dictyostelium* PI3K1/2 cells, where PIP3 production is severely impaired^{61,64}, the R(+8)-Pre profile remained strongly complementary to front-state sensors for actin polymerization (Fig. 3n) and Ras activation (Fig. 3o). These results demonstrate that PIP3 does not substantially contribute to the membrane surface charge.

A decreased net surface charge triggers protrusions and abrogates polarity

The dynamic patterns of the surface charge suggests that it could serve as a biophysical organizer of signalling and cytoskeletal networks. These networks have been previously modelled as excitable systems consisting of both positive- and delayed negative-feedback loops^{56,65–68}. It has been suggested that the delayed negative-feedback loop includes the action of substrates of AKTs and other refractory molecules^{56,69}. The positive feedback was implemented as a mutually inhibitory

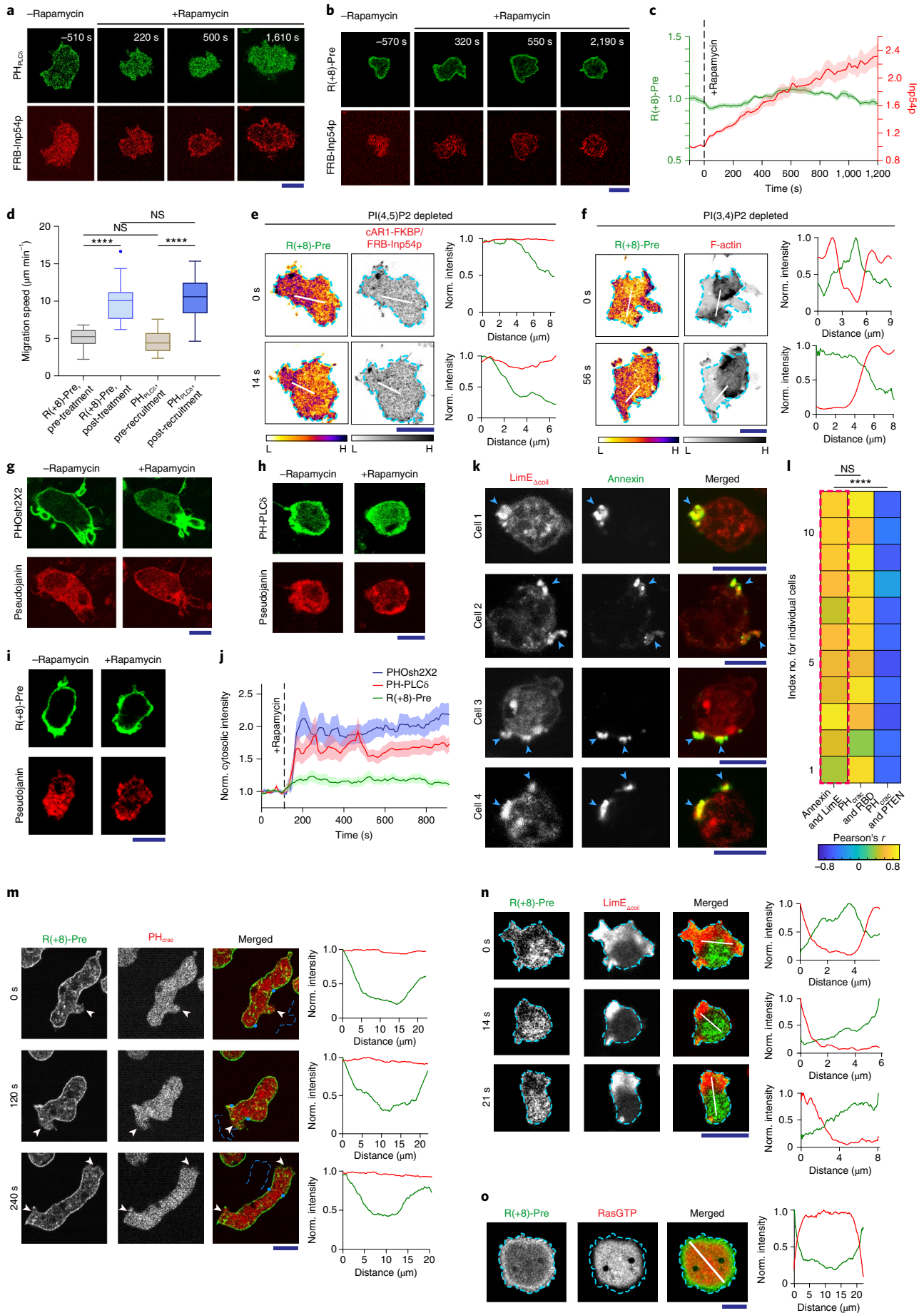
interaction between the front and back states, consisting of Ras and Rap, and PI(4,5)P2 and PI(3,4)P2, respectively, given that induced decreases in these lipids activated the network^{3,37}. However, we considered these effects might be attributable to decreases in the surface charge rather than the signalling properties of these lipids (Fig. 4a). In this scenario, the activated state would decrease the surface charge, while a decreased negative surface charge would lead to activation (Fig. 4a). To test this concept, we developed two non-specific actuators to acutely decrease or increase the negative surface potential profile via optogenetic recruitment (Fig. 4b). Consisting of a short-chain of charged amino acids, these actuators (unlike conventional GEF/GAP/RGS/kinase/phosphatase-based actuators^{70–74}) are not directed at any particular biochemical reaction.

The first actuator, designated Opto-ACTU⁺, had a net charge of +16 (Fig. 4c). Following spatially restricted recruitment from the cytosol to the membrane (Fig. 4d), it should locally reduce the net negative surface charge on the inner membrane and thereby increase the positive feedback there (Fig. 4a). That would increase the probability of spontaneous firing and de novo protrusion generation. When Opto-ACTU⁺ was recruited to a quiescent back region of a polarized *Dictyostelium* cell, new protrusions indeed started forming nearby (Fig. 4e, Extended Data Fig. 7a and Supplementary Video 8), resembling the effects of previously reported specific perturbations of signalling molecules (such as Rac1, Cdc42 and GPCR opsins)^{75–77}. With the recruitment of uncharged Opto-CTRL, new protrusions rarely appeared near the irradiation area (Fig. 4f, Extended Data Fig. 7b and Supplementary Video 8), indicating that the protrusion formation was due to the reduction in surface charge and not irradiation or cryptochrome recruitment. The angular histograms demonstrate that the probability of new protrusion generation was highest in the vicinity of the Opto-ACTU⁺ recruitment (Fig. 4g), whereas Opto-CTRL recruitment did not induce a bias (Fig. 4h).

We anticipated that when Opto-ACTU⁺ was globally recruited in polarized cells, more protrusions would be generated and polarity would be disrupted. Within a few minutes of global recruitment of Opto-ACTU⁺, cells began to extend protrusions rapidly all along the cortex (Fig. 5a,b and Supplementary Video 9), including from domains of erstwhile back states. Consequently, polarity was abrogated (Fig. 5c) and migration was impaired (Fig. 5d,e). The number of new protrusions increased about 2.5-fold (Fig. 5f), which theoretically is consistent with the amount of surface-charge reduction (Supplementary Notes 1 and 2). If the 488-nm laser was switched off and recruited Opto-ACTU⁺ was allowed to return to the cytosol, then the cells repolarized and resumed migration (Fig. 5g and Supplementary

Fig. 3 | Dynamics of the inner-membrane surface-charge sensor R(+8)-Pre in different anionic phospholipid-depleted cells. a, b, The dynamics of the membrane localization of PH_{PLC6}-GFP (**a**) and GFP-R(+8)-Pre (**b**) before and after PI(4,5)P2 depletion in *Dictyostelium* cells by recruiting mCherry-FRB-Inp54p to membrane-bound cARI-FKBP. Rapamycin was added at $t = 0$ s. **c**, Time course of the normalized membrane-to-cytosol intensity ratio of R(+8)-Pre and Inp54p following rapamycin addition (indicated by the dashed vertical line). Data are the mean \pm s.e.m. (indicated by the lighter shading); $n_c = 20$ cells. **d**, Migration speed, before and after the addition of rapamycin, of cells coexpressing the same chemically inducible dimerization system for PI(4,5)P2 depletion along with either GFP-R(+8)-Pre or PH_{PLC6}-GFP; $n_c = 32$ cells tracked for $n_f = 60$ frames per group. The box-and-whisker plots were graphed using Tukey's method. **e**, Spatiotemporal back localization of R(+8)-Pre in PI(4,5)P2-depleted cells shown in the 'fire invert' colourmap of Fiji/ImageJ. Inp54p recruited to the uniform membrane anchor cARI is symmetrical in the ventral waves (middle). **f**, Complementary localization of GFP-R(+8)-Pre and LimE-mCherry (biosensor for newly polymerized F-Actin) in the ventral waves of *DdSp4* *Dictyostelium* cells. **e, f**, L, low; and H, high. **g–i**, Live-cell images of RAW 264.7 macrophages showing the membrane localization profile of the PI4P biosensor PHOsh2X2-GFP (**g**), PI(4,5)P2 biosensor PH_{PLC6}-GFP (**h**) and GFP-R(+8)-Pre (**i**) before and after pseudojanin recruitment to the membrane anchor Lyn-FRB-CFP. **j**, Time course of the normalized cytosolic intensity of

PHOsh2X2, PH_{PLC6} and R(+8)-Pre following the addition of rapamycin (indicated by the dashed vertical line). Data are the mean \pm s.e.m. (indicated by the lighter shading). PHOsh2X2, $n_c = 16$ cells; PH_{PLC6}, $n_c = 10$ cells; and R(+8)-Pre, $n_c = 12$ cells. **k**, Representative examples of protrusion-forming *Dictyostelium* cells expressing LimE-GFP whose outer leaflet of the membrane was allowed to transiently bind with annexin V-Alexa Fluor 488. Blue arrowheads are pointing to protrusion areas where outer leaflet PS as well as LimE was enriched. **l**, Heatmap of Pearson's r between annexin V and LimE (left; dashed red rectangle). The r values for comparisons between PH_{crac} and RBD (middle), and PH_{crac} and PTEN (right) are shown to demonstrate standard co- and counterlocalization profiles. Correlation coefficients were calculated along the cell membrane; $n_c = 11$ cells per group. **m**, Live-cell images of a LY294002-treated migrating *Dictyostelium* cell coexpressing GFP-R(+8)-Pre and PH_{crac}-mCherry. The white arrowheads point to protrusions where PIP3 was depleted but the surface charge gradient was maintained. The line scans along the dashed blue lines are shown in the right panels (blue dots show the end points of the blue lines on the cell membrane). **n, o**, Live-cell images of ventral waves in PI3K1/2 *Dictyostelium* cells coexpressing GFP-R(+8)-Pre and the front-state markers LimE-mCherry (**n**) or RBD-mCherry (**o**). **d, l, i**, P values were determined using a Mann-Whitney-Wilcoxon test; NS, not significant ($P > 0.05$) and **** $P \leq 0.0001$. **e, f, n, o**, Line scans of all ventral waves along solid white lines are shown on the right. Norm., normalized. Scale bars, 10 μ m. Source numerical data are provided.



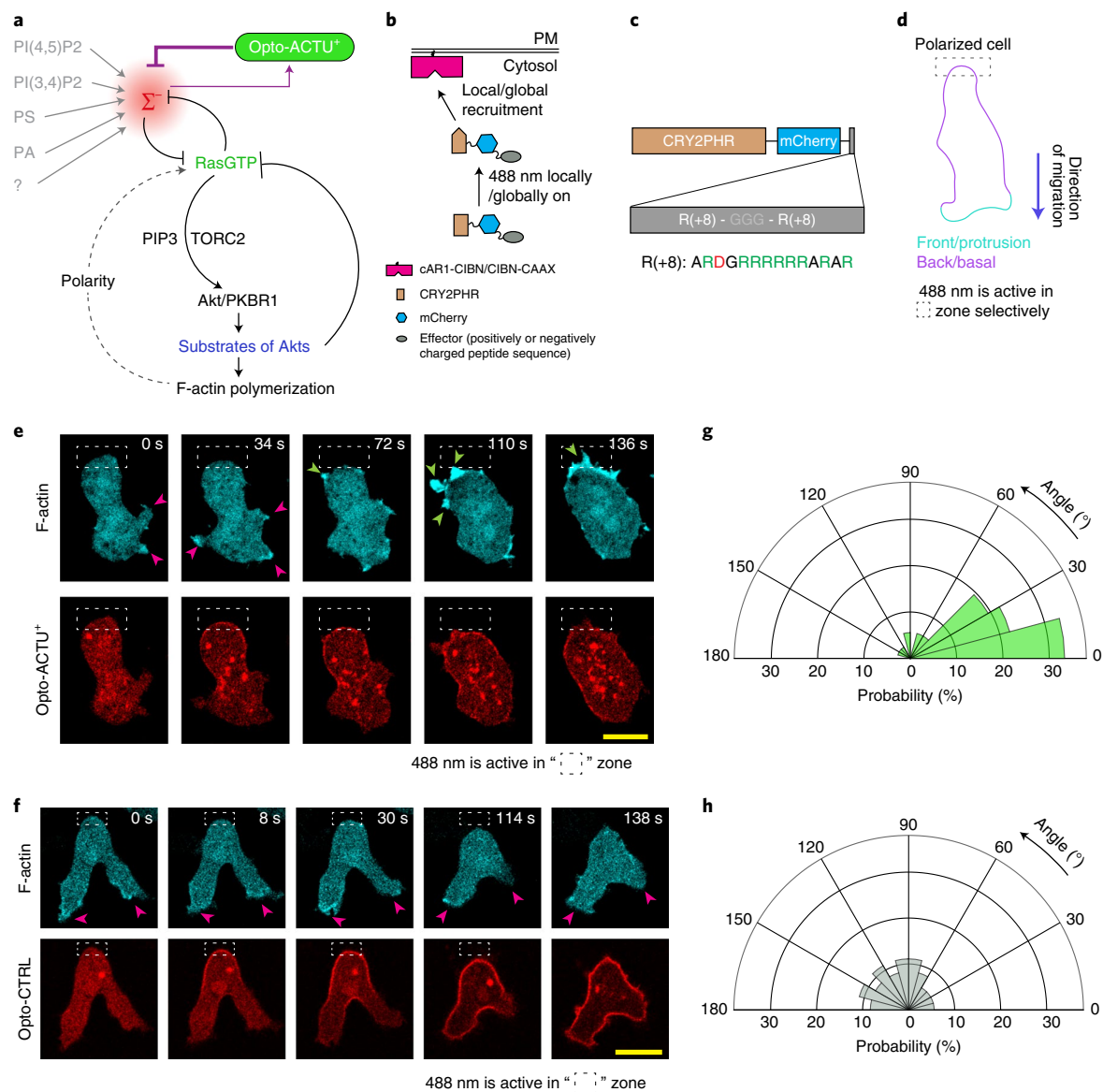


Fig. 4 | Localized lowering of the membrane surface charge can trigger de novo protrusion generation from the area of the reduced surface charge.

a, Schematic for lowering negative surface charge through the recruitment of a positively charged optogenetic actuator, Opto-ACTU⁺, in the context of overall biochemical excitable network topology. Σ^- , back state defined by an overall negative surface charge. Opto-ACTU⁺ interferes with the topology by associating with Σ^- but in turn provides negative feedback to Σ^- . **b**, Schematic for optogenetic actuator recruitment. Illumination with a 488-nm laser changes the conformation of the cytosolic cryptochrome module and as a result CRY2PHR, along with its associated positively or negatively charged peptide, gets recruited to the plasma membrane-bound CIBN. CIBN-CAAX was used in all mammalian systems as a membrane anchor and cARI-CIBN was used in all *Dictyostelium* experiments. **c**, Design of Opto-ACTU⁺ with a net charge +16. Positively charged amino acids are shown in green and negatively charged amino

acids in red. **d**, Experimental set-up of selective optical recruitment at the back of polarized *Dictyostelium* cells. **e**, Representative time-lapse images of selective de novo protrusion formation from the area of recruitment in *Dictyostelium* cells coexpressing Opto-ACTU⁺, cARI-CIBN and LimE-Halo. **f**, Representative time-lapse images of *Dictyostelium* cells coexpressing Opto-CTRL, cARI-CIBN and LimE-Halo demonstrating that locally restricted recruitment of Opto-CTRL did not generate new protrusions from the site of recruitment. **e, f**, The dashed rectangle shows the area where a 488-nm laser was selectively illuminated for recruitment; the magenta and green arrowheads point to existing and newly induced protrusions, respectively. Scale bars, 10 μm . **g, h**, Polar histogram of the angle of protrusion formation with respect to the recruitment area for Opto-ACTU⁺ (**g**) and Opto-CTRL (**h**) recruitment. Probabilities were calculated for $n_c = 23$ (**g**) and 20 (**h**) cells, and $n_p = 36$ protrusions (**g, h**). Source numerical data are provided.

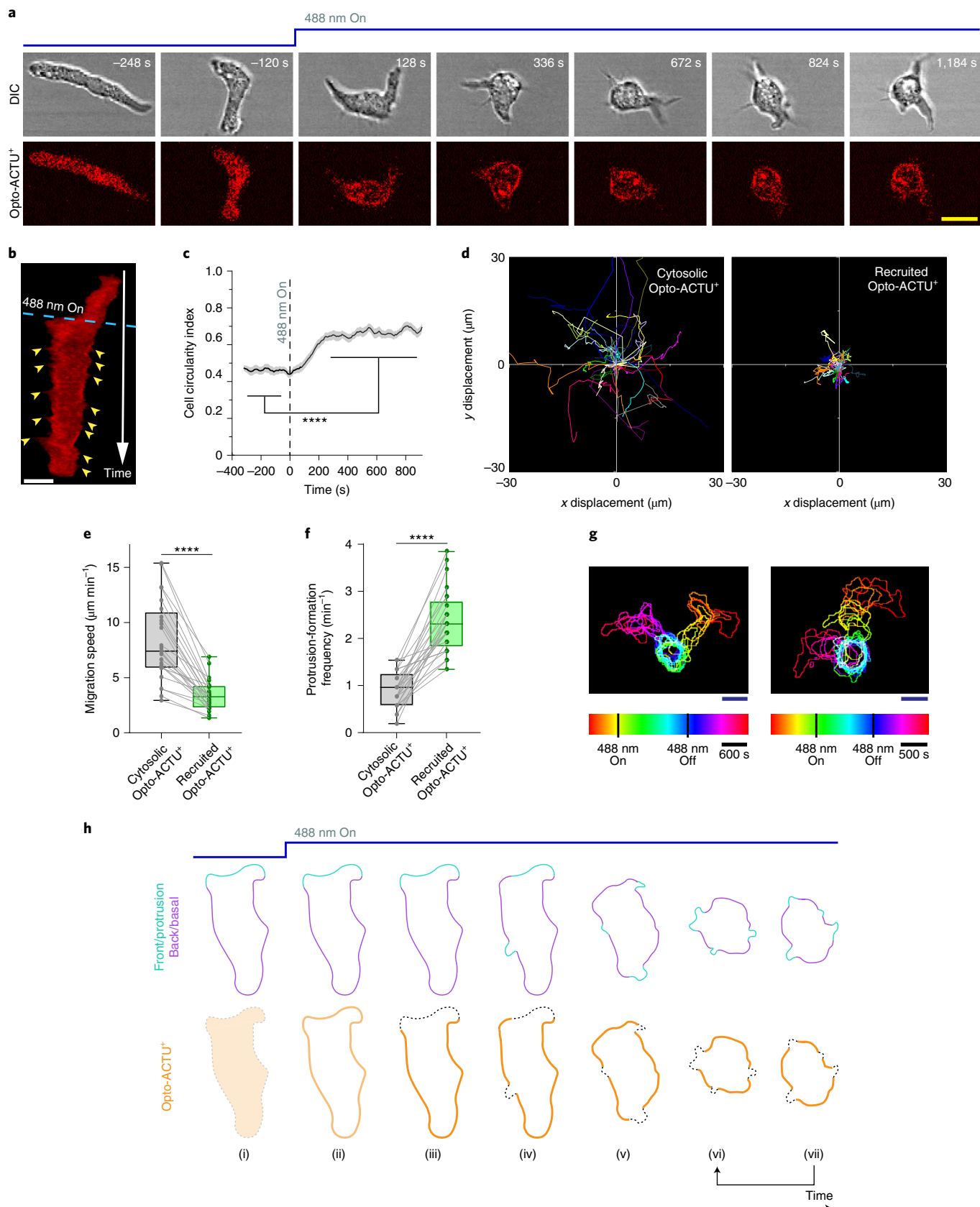
Video 10). No consistent changes in polarity, migration or protrusion formations were observed following recruitment of the uncharged Opto-CTRL (Extended Data Figs. 7c, d and Supplementary Video 9), as quantified in terms of the cell circularity index (Extended Data Fig. 7e), speed (Extended Data Figs. 7f, g) and protrusion-formation frequency (Extended Data Fig. 7h).

Careful observation revealed that, in addition to the increase in protrusion formation induced by the recruitment of the Opto-ACTU⁺, a series of events was occurring: as new protrusions/front-state

regions established, recruited Opto-ACTU⁺ quickly moved away from these regions (Fig. 5a, b and Supplementary Video 9) and gradually accumulated towards other back-state regions. This accumulation triggered another protrusion there and the entire cycle was repeated (Fig. 5h).

Surface charge alters migration and polarity through signalling and cytoskeleton networks

To investigate the molecular mechanisms through which membrane surface charge acts, we used a series of genetically encoded



biosensors as well as different pharmacological and genetic perturbations in conjunction with our optogenetic actuators (Fig. 6a). First, when Opto-ACTU⁺ was recruited, it accumulated to the existing back-state regions of the cortex and actin polymerization was eventually initiated

there (Fig. 6b). The local accumulation of Opto-ACTU⁺ consistently preceded actin polymerization (Fig. 6b and Extended Data Fig. 8a,b). Next, we monitored the activation and localization kinetics of different upstream signalling molecules during perturbations of the surface

Fig. 5 | Global lowering of the negative surface charge of the membrane can abolish the pre-existing polarity by consistently generating new protrusions from the back-state regions. **a,b**, Time-lapse snapshots (**a**) and time stack (**b**) demonstrating changes in cell morphology and migration mode of a polarized *Dictyostelium* cell coexpressing Opto-ACTU⁺ and cARI-CIBN following the recruitment of Opto-ACTU⁺. The 488-nm laser was switched on globally at $t = 0$ s. **a**, DIC, differential interference contrast microscopy. **b**, The yellow arrowheads point to newly generated protrusions. Note that Opto-ACTU⁺ is consistently depleted in the protrusions. **c–f**, Cell-morphology and migration-mode changes, in terms of the circularity index of the cell (**c**), cell tracks (**d**), migration speed (**e**) and frequency of the formation of new protrusions (**f**), following Opto-ACTU⁺ recruitment ($n_c = 25$ cells). **c**, Data are the mean \pm s.e.m. (indicated by the lighter shading). **d**, Tracks were reset to the same origin. **d–f**, Each cell was tracked for $n_t = 40$ frames both before and after recruitment (image acquisition frequency of 8 s per frame). For pairwise comparisons, the tracks are colour-coded in **d** and data from same cell are connected by grey lines in **e,f**. The box-and-whisker plots were graphed using Tukey's method in **e,f**. *P* values

were determined using a Mann–Whitney–Wilcoxon test; **** $P \leq 0.0001$. **g**, Two representative examples of temporally colour-coded cell outlines showing the cell morphology and migratory modes before, during and after illumination with a 488-nm laser. **h**, Schematic proposing how Opto-ACTU⁺ recruitment changes the cell morphology and migratory mode. (i),(ii), Opto-ACTU⁺ is recruited globally as expected; (iii) however, presumably due to its positive charge, it quickly accumulates along the back regions of the cell. (iv),(v), Consequently, new protrusions are elicited from these back regions and the cell begins to lose polarity. (iv)–(vii), At the same time, as some areas of erstwhile back regions are converted to front regions, Opto-ACTU⁺ redistributes again to the newly formed back regions. This in turn generates fresh protrusions there and this entire cycle is repeated (shown in arrows between (vi) and (vii)). As a result, protrusions are generated randomly, migration becomes impaired and pre-existing polarity is abrogated. The dashed black lines in the Opto-ACTU⁺ channel indicates depletion of recruited Opto-ACTU⁺ from protrusions (**h**). Scale bars, 10 μ m (**a,b,g**); temporal scale bars, 600 s (**h**(left)) and 500 s (**h**(right)). Source numerical data are provided.

charge. Localization of Opto-ACTU⁺ to a spatially confined domain within the back states of the membrane consistently caused dissociation of the established back protein PTEN from that domain (Fig. 6c and Extended Data Fig. 8c). Using the standard biosensors for PIP3 and GTP-bound Ras, we found that PI3K (Extended Data Fig. 8d,e) and Ras (Fig. 6d and Extended Data Fig. 8f) were dynamically activated in the membrane domains where the surface charge was lowered.

Next, we modified different nodes of the Ras/PI3K/TORC2/Akt/F-actin network using genetic knockouts and drug treatments to interfere with the Opto-ACTU⁺-mediated increase in protrusion formation (Fig. 6a). First, in *PTEN*[−] *Dictyostelium* cells, which have elevated PIP3 levels, increased protrusions and impaired migration^{78–80}, recruitment of Opto-ACTU⁺ induced even more frequent protrusions (Fig. 6e and Extended Data Fig. 9a), which further impaired migration (Fig. 6f and Extended Data Fig. 9b,c). Reduction of PIP3 through pre-treatment with LY294002 (refs. 60–63) only slightly inhibited the Opto-ACTU⁺ recruitment-driven phenotypic changes in the protrusion frequency (Fig. 6e and Extended Data Fig. 9d) and migration speed (Fig. 6f and Extended Data Fig. 9e). When both PTEN and PI3K activity were impaired, recruitment of Opto-ACTU⁺ still increased protrusion formation (Fig. 6e and Extended Data Fig. 9f), slowed migration (Fig. 6f and Extended Data Fig. 9g,h) and reduced polarity (Extended Data Fig. 9i and Supplementary Video 11). Thus, although a reduction in surface charge is normally associated with PI3K activation and membrane dissociation of PTEN, the phenotypic changes could be still induced in the absence of these activities. This observation does not completely rule out a role for PIP3 given that the inhibition may not be complete and other enzymes may substitute for PTEN^{64,79,81}. Standalone inhibition of TORC2 by PP242 (refs. 9,82) only

slightly hindered the Opto-ACTU⁺ recruitment-driven migration phenotypic changes (Fig. 6e,f and Extended Data Fig. 9j,k). On the other hand, inhibition of both PI3K and TORC2 with a cocktail of LY294002 and PP242 almost completely blocked the induced change in protrusion formation and migration speed (Figs. 6e,f and Extended Data Fig. 9l,m). Given that PI3K and TORC2 act together to activate the AKT and AKT-related kinase PKBRI (refs. 9,61,62), we studied the effect of optogenetic perturbation in *Akt*[−] *PKBRI*[−] cells. The Opto-ACTU⁺ recruitment-induced phenotypic changes did not occur in these cells (Fig. 6e,f and Extended Data Fig. 9n,o). Together, these findings suggest that surface charge-mediated changes in migration or protrusion formation act via the collective action of the Ras/PI3K/TORC2/AKT/F-actin network.

Addition of actuators to excitable network simulations mimics the observed phenotypes

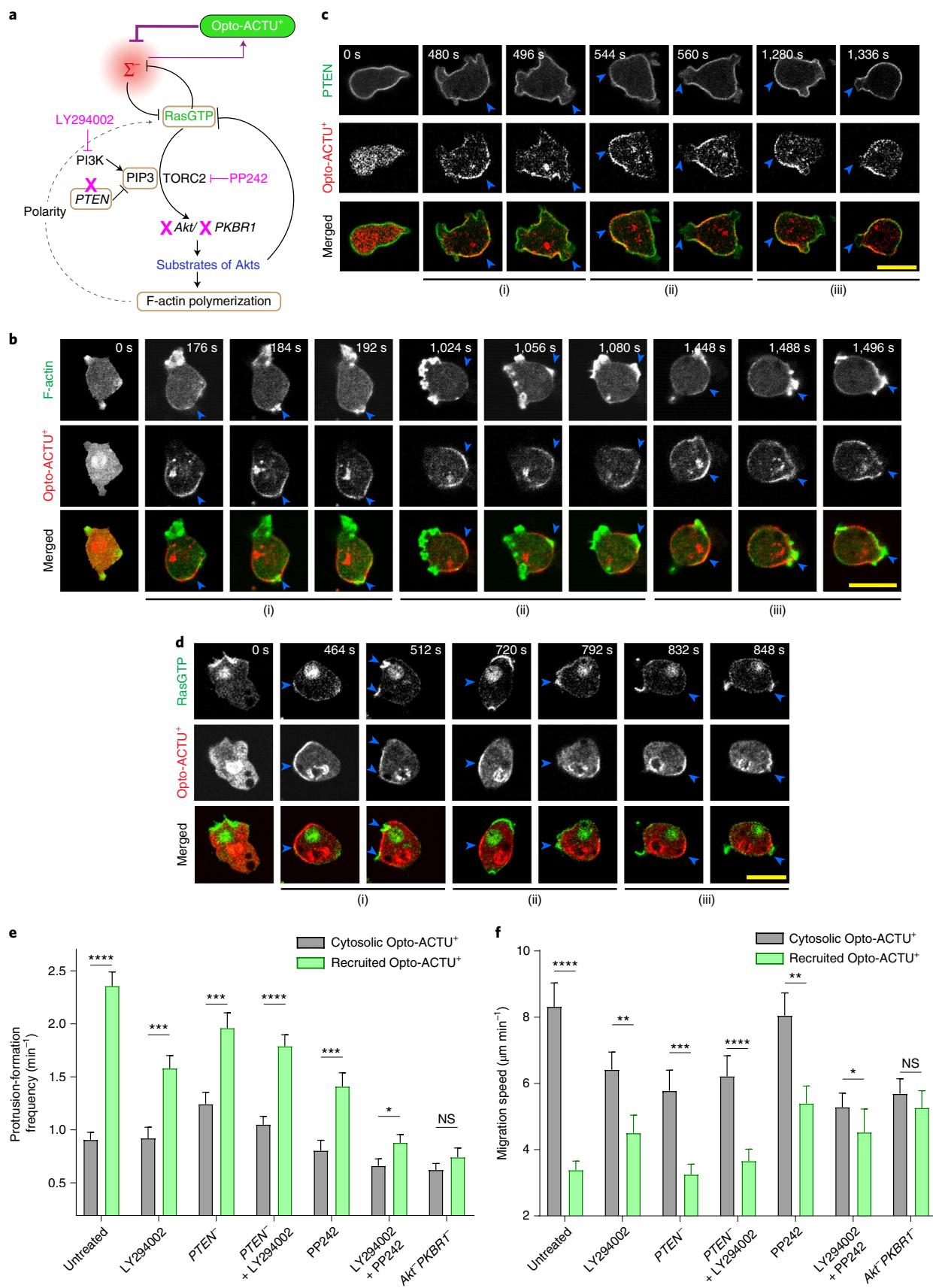
To simulate these polarity-breaking and protrusion-formation phenomena, we incorporated separate actuator dynamics into a model of the excitable network that includes polarity⁸³ (Supplementary Note 1 and Fig. 7a–c). Before incorporating perturbations, polarity biased the excitable network, resulting in persistently localized firings, which underlie protrusions (Fig. 7d). Following simulated recruitment, Opto-ACTU⁺ lowered the threshold and caused abrupt increases in overall activity along the whole perimeter. With the development of each front-state region, Opto-ACTU⁺ quickly redistributed to new back-state regions, where it reduced the local threshold and as a result triggered new protrusions (Fig. 7d,e). As in experiments, this cycle repeated. Reversibility of this actuation process was also recreated in the simulations by allowing the actuators to dissociate from the membrane (Fig. 7f,g). We also simulated the selective protrusion formation by

Fig. 6 | The phenotypic changes induced by Opto-ACTU⁺ recruitment are mediated by the Ras/PI3K/Akt/TORC2/F-actin network. **a**, Schematic showing nodes of the signalling and cytoskeletal network that were monitored and/or perturbed in conjunction with Opto-ACTU⁺ recruitment. Tan-coloured rectangles, molecules whose dynamics were recorded; magenta blocked arrows, pharmacological inhibition; and magenta crosses, genetic knockout. **b**, Live-cell images of *Dictyostelium* cells coexpressing Opto-ACTU⁺, cARI-CIBN and LimE–GFP. Recruitment was started at $t = 0$ s. Three representative actin-polymerization cases are shown ((i)–(iii)). For each case, three events are shown: first, Opto-ACTU⁺ accumulated inside a domain of the membrane; second, F-actin polymerization was initiated there and finally, when that domain fully turned into the front state, Opto-ACTU⁺ moved away from that domain. Blue arrowheads point to membrane domains where Opto-ACTU⁺ was first accumulated and where back states were replaced by front events. **c,d**, Live-cell images of *Dictyostelium* cells coexpressing Opto-ACTU⁺ and cARI-CIBN along with PTEN–GFP (**c**) or RBD–GFP (**d**). Recruitment was started at $t = 0$ s. Three representative cases ((i)–(iii)) of

PTEN dissociation from the membrane (**c**) and Ras activation on the membrane (**d**) are shown. For each case, two events are shown: first, the accumulation of recruited Opto-ACTU⁺ inside a domain of the membrane and second, when that accumulation resulted in the dissociation of PTEN (as in **c**) and Ras activation (as in **d**) in that particular domain (which in turn caused Opto-ACTU⁺ to move away from there). **e,f**, Phenotypic changes following Opto-ACTU⁺ recruitment, in terms of the frequency of new protrusion formation (**e**) and migration speed (**f**), in the presence of different pharmacological inhibitors or genetic knockouts. Untreated and LY294002, $n_c = 28$ cells; PP242 and *PTEN*[−], $n_c = 22$ cells; *PTEN*[−] + LY294002, $n_c = 24$ cells; LY294002 + PP242, $n_c = 27$ cells; and *Akt*[−] *PKBRI*[−], $n_c = 21$ cells. For each treatment group, each of the n_c cells were tracked for $n_t = 40$ frames (8 s per frame) and time averages were taken. Data are the mean \pm s.e.m. *P* values were determined using a Mann–Whitney–Wilcoxon test. NS, not significant ($P > 0.05$); * $P \leq 0.05$; ** $P \leq 0.01$; *** $P \leq 0.001$ and **** $P \leq 0.0001$. For pairwise comparisons and more detailed data, see Supplementary Fig. 9. Scale bars, 10 μ m. Source numerical data are provided.

confining the recruitment of the actuator within a back-state region and observed increased activity there, which resulted in a switch in polarity and the usual eventual actuator rearrangement (Fig. 7h). Together,

these findings suggest that during polarized cell migration, a higher negative surface charge at the back-state regions leads to an increased threshold, which prevents protrusion formation there.



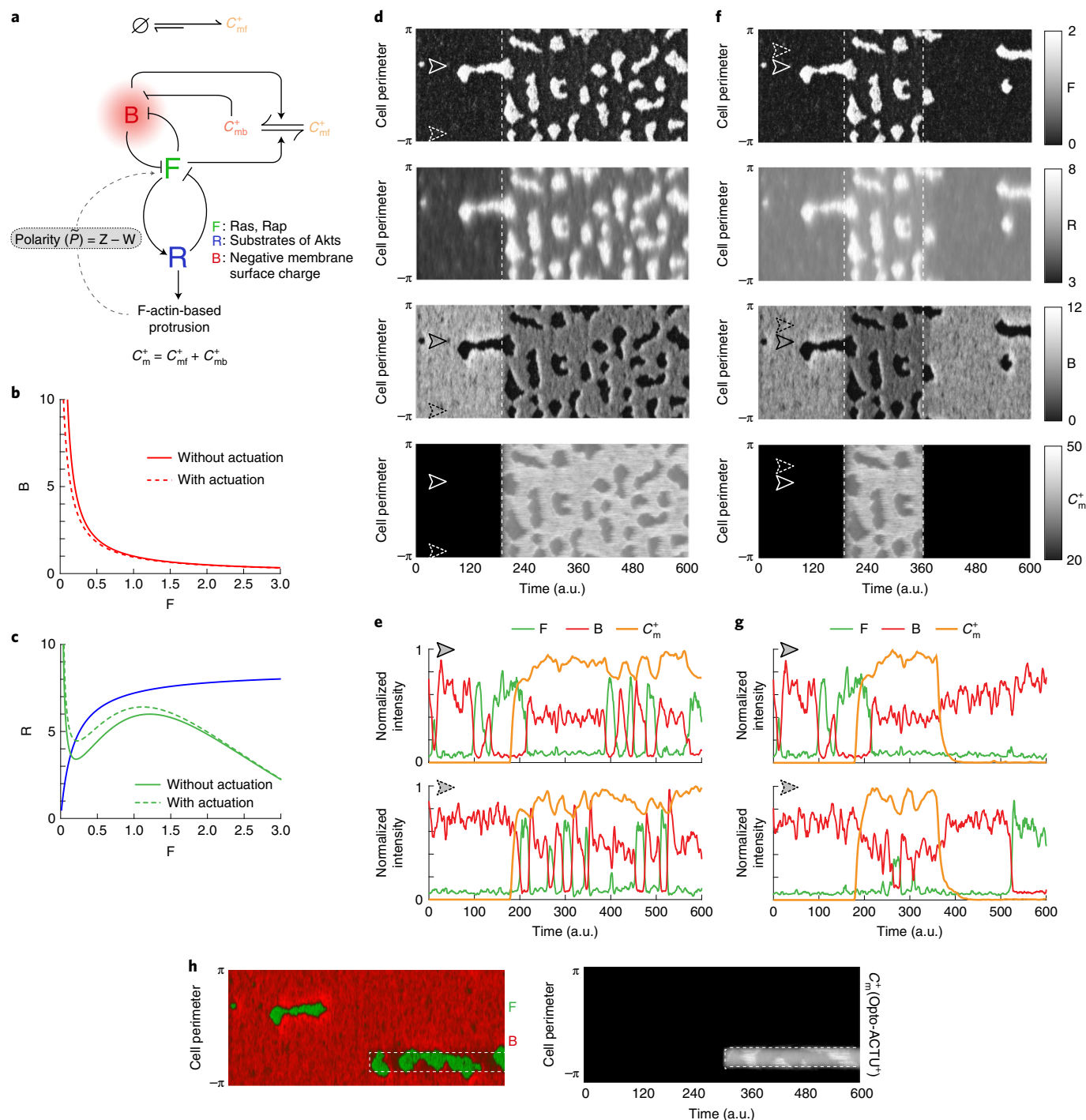


Fig. 7 | In silico reduction of the membrane surface charge recreates the polarity breaking and demonstrates increased activity over the membrane. **a**, Schematic showing the coupled system of excitatory network, polarity module (comprised of the local activator Z and delayed globally diffusing inhibitor W) and the Opto-ACTU⁺ (C_m^+) system. The excitable network involves membrane states F (front), B (back; defined by the overall surface charge of the inner membrane) and R (refractory). The Opto-ACTU⁺ system constitutes of the fast-diffusing state C_{mf}^+ and the almost stationary membrane-bound state C_{mb}^+ . The total charge actuator C_m^+ on the membrane is the summation of both the fast-diffusing and membrane-bound states. **b**, Plot of B versus F with and without Opto-ACTU⁺. **c**, F (green lines) and R (blue line) nullclines with and without Opto-ACTU⁺ (under the steady-state assumption for B). **d**, The simulated kymographs of F (first), R (second), B (third) and C_m^+ (fourth) in response to global recruitment. The instant of recruitment is shown by the white dashed line. **e**, Line

scans at two locations (denoted by dashed and solid arrowheads) on the simulated kymographs in **d** showing the temporal profiles of F, B and C_m^+ . **f, g**, In silico reversible recruitment of Opto-ACTU⁺ demonstrating the reversibility of polarity-breaking and protrusion-formation events. **f**, Simulated kymographs. The instant of recruitment is shown by the first white dashed line and the second dashed line shows when recruitment was stopped. **g**, Line scans at two locations (denoted by dashed and solid arrowheads) in **f**. **h**, Simulated kymographs of membrane states in response to the selective recruitment of Opto-ACTU⁺ (C_m^+). Merged views of F and B (left) and the profile of Opto-ACTU⁺ (C_m^+ ; right) are shown. The same timescale is applicable in both the left and right panels. The white dashed box indicates the location of in silico selective recruitment. Note that simulated selective recruitment created a de novo front state around the recruitment area, which in turn caused the recruited actuator to move away (as happened in global recruitment). a.u., arbitrary units.

Locally elevated surface charge suppresses protrusions

Given that a reduction in the negative surface charge was able to activate the signalling network, we investigated whether its direct elevation can deactivate the network and limit protrusions (Fig. 8a). To test this, we designed a second optogenetic peptide, Opto-ACTU⁻, with a net charge of -14, which is expected to increase the negative surface charge on the inner membrane upon recruitment (Fig. 8b). We chose RAW 264.7 macrophages as they are generally quiescent but can be globally activated by a C5a-receptor agonist to induce protrusions all along the membrane. We first recruited Opto-ACTU⁻ to a confined region to increase the local negative surface charge and then globally stimulated the cell with a C5a-receptor agonist (Fig. 8c). Protrusions formed along the membrane except in the vicinity of the recruitment region (Fig. 8d, Extended Data Fig. 10a and Supplementary Video 12). This induced a polarity in the cell and the cell slowly migrated away (Fig. 8d, Extended Data Fig. 10a and Supplementary Video 12), resembling the migration phenotype caused by direct perturbations of signalling molecules^{16,84}. Compared with Opto-ACTU⁻ (Fig. 8e), local recruitment of Opto-CTRL could not suppress agonist-induced protrusions (Extended Data Fig. 10b and Supplementary Video 12) and the protrusion-formation probability remained uniform (Extended Data Fig. 10c). In simulations, when we locally elevated the threshold mimicking Opto-ACTU⁻ recruitment and superimposed a global reduction of threshold representing receptor input (Extended Data Fig. 10d), activity increased everywhere except where the local suppression was enforced (Fig. 8f and Extended Data Fig. 10e).

Increased surface charge subverts EGF-induced ERK activation

We next investigated whether increases in the negative membrane surface potential can override the epidermal growth factor (EGF) receptor-mediated activation of ERK given that the pathway involves Ras activation (Fig. 8g). MCF10A cells were first activated with a saturating dose of EGF, which was confirmed by the predominantly cytosolic distribution of the ERK-activation sensor ERK-KTR (Fig. 8h, first time point; Extended Data Fig. 10f, first time point; and Supplementary Video 13). When we increased the surface charge of the membrane by globally recruiting Opto-ACTU⁻ (Fig. 8g), a substantial fraction of ERK-KTR became nuclear, indicating a deactivation of ERK (Fig. 8h and Supplementary Video 13), whereas control Opto-CTRL recruitment caused no detectable effect (Extended Data Fig. 10f and Supplementary Video 13). Quantitation of multiple cells showed that, despite some fluctuations in ERK activity (Extended Data Fig. 10g,h), Opto-ACTU⁻ recruitment provoked an increase of approximately 50% in the nucleus/cytosol ratio of ERK-KTR compared with the uncharged control (Fig. 8i).

Discussion

Our study suggests that negative surface charge, or zeta potential, on the inner leaflet of the membrane coordinates the activities of the Ras/PI3K/TORC2/F-actin networks that control cell migration and polarity. Under physiological conditions there is a spontaneous reduction in charge during network activation at protrusions and within front-state regions on the ventral waves of cells. Decreases in the levels of PI(4,5)P₂, PI(3,4)P₂, PS and PA collectively contribute to this charge reduction. An altered membrane surface charge is necessary and sufficient for network activation and is not a merely a consequence of it, given that the recruitment of a positively charged actuator to the membrane activates the network, whereas recruitment of a negatively charged actuator to the membrane prevents the chemoattractant or growth factor-stimulated activation. Our results suggest that the surface charge of the inner membrane is a key biophysical parameter that appears within the feedback loops determining the setpoint of these networks.

Our data indicate that the fluid-mosaic model of the membrane is more complex than originally envisioned. Large patches of multiple anionic lipids and peripheral membrane proteins co-segregate into defined 'phase' domains that propagate as waves. For phosphoinositides and peripheral membrane proteins, wave propagation is probably mediated by sequential transient modification of the lipid headgroups and shuttling of the proteins^{39,67,68,85,86}. For example, local transient increases in PIP₃ occur where PI3K is briefly activated by Ras^{87,88} and PTEN reversibly dissociates^{78,89}. Detailed studies will be needed to determine which kinases and phosphatases are sequentially activated or inhibited to control the levels of PI(4,5)P₂, PI(3,4)P₂ and PA in the membrane. Based on our initial data showing that PS is regulated by dynamic externalization, we anticipate that flippases, floppases or scramblases whose activation tracks closely with activation of the Ras/PI3K/TORC2/F-actin network will be identified in future.

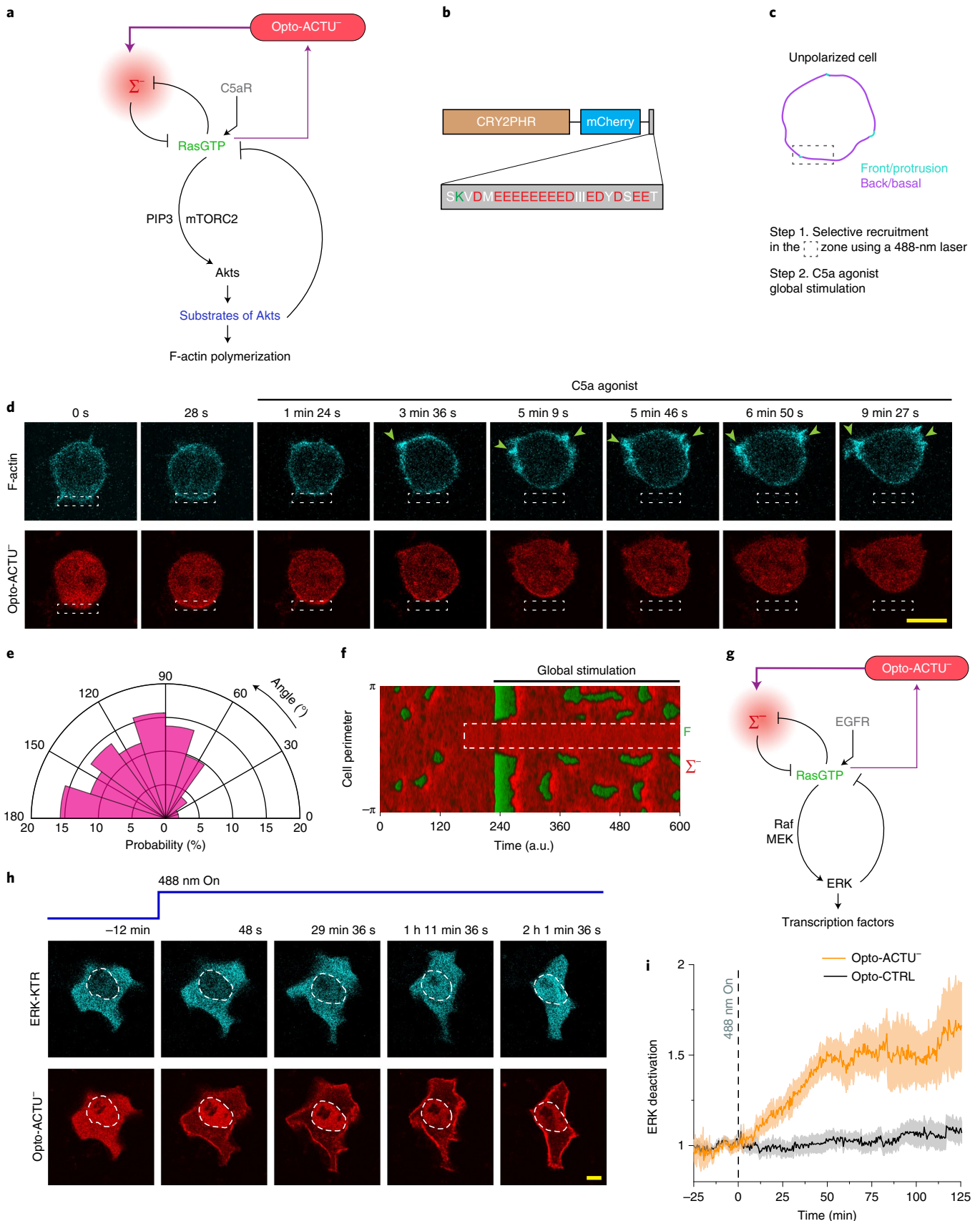
Optogenetic actuators enabled generic alteration of surface charge inside live cells with spatiotemporal control. The observed effects on cell behaviour suggest that an induced biophysical change, that is, a reduction in zeta potential, sets in motion a series of biochemical events involved in motility and polarity. To our knowledge, an effect of direct surface-charge perturbation on signalling and cytoskeletal events has not been reported. Traditional approaches with isolated membranes^{29,34,90–92}, giant unilamellar vesicles/liposomes or charged surfactant typically cannot accurately mimic the physiological environment inside cells. Other recent methods^{21,22,50}, such as phosphoinositide degradation/synthesis by chemically induced dimerization or different pharmacological perturbations (which change the calcium/ATP levels), do not provide spatial control or decouple the surface charge from other cell physiological changes. Given that our novel actuators can work

Fig. 8 | Increased negative surface potential in the inner membrane suppresses protrusions in macrophages and, separately, deactivates EGF-induced ERK activity in epithelial cells. **a**, Schematic for the elevation of the negative surface charge on the plasma membrane through the recruitment of the negatively charged optogenetic actuator Opto-ACTU⁻ in the context of biochemically excitable network topology with receptor input. **b**, Design of Opto-ACTU⁻ with a net charge of -14. Positively charged amino acids are shown in green and negatively charged amino acids in red. **c–e**, Experimental set-up of selective Opto-ACTU⁻ recruitment, followed by uniform C5a stimulation, in unpolarized RAW 264.7 macrophages (**c**); representative time-lapse images demonstrating cell migration driven by selective suppression of protrusion in the site where Opto-ACTU⁻ was locally recruited and protrusion formation in other areas of cortex following uniform C5a stimulation (**d**); and polar histogram indicating a higher probability of protrusion formation away from the recruitment area. Cells coexpressing Opto-ACTU⁻, CIBN-CAAX and Lifeact-mVenus were used. **d**, The green arrowheads point to F-actin-rich protrusions

marked by Lifeact. **e**, $n_c = 12$ cells and $n_p = 51$ protrusions. **f**, Simulated kymograph of membrane states in response to the in silico recruitment of Opto-ACTU⁻ (C_m^-), followed by global stimulation. **F**, front state; Σ^- , back state; and a.u., arbitrary units. **g**, Schematic for the elevation of negative surface charge in the context of excitable network-mediated ERK regulation along with the receptor input module. **h**, Representative time-lapse images of an MCF10A cell displaying ERK-KTR translocation from the cytosol to the nucleus demonstrating ERK deactivation following global Opto-ACTU⁻ recruitment to the membrane. Cells that were coexpressing Opto-ACTU⁻, ERK-KTR-iRFP713 and CIBN-CAAX were pre-treated with, and maintained in, a saturating dose of EGF throughout the experiment. Shapes with dashed white lines are showing the nucleus of the cell. **i**, Levels of ERK deactivation in terms of the normalized ERK-KTR nucleus/cytosol ratio. Data are the mean \pm s.e.m. (indicated by lighter shading); $n_c = 12$ cells per group (Opto-ACTU⁻ and Opto-CTRL); illumination with a 488-nm laser was initiated at $t = 0$ min (as shown by the vertical dashed line). Scale bars, 10 μ m. Source numerical data are provided.

orthogonally to external cues—such as chemoattractant gradients and/or external electric fields—and act at the inner membrane, they can potentially unravel the molecular architecture of biochemical

networks in other physiological scenarios such as immune-synapse formation and phagocytosis (and others that are likely to be found in the future) where surface-charge remodelling takes place.



Our study establishes surface potential as an organizer of signal transduction and cytoskeletal events that control cell migration and polarity. We suggest the term ‘action surface potentials’ to describe the travelling membrane domains of transiently decreased negative surface charge. We propose that a high negative surface charge corresponds to a ‘resting’ or back state of the membrane, whereas the regions of decreasing surface charge are transitioning to an active/front state that leads to protrusions. We envision that as the surface charge decreases, molecules that regulate the signalling activities respond differentially. Further studies are needed to determine which crucial network components may be directly regulated by charge. We show here that PTEN back-state localization is largely determined by its positively charged amino terminus (which is also necessary for membrane binding^{79,93}) and other peripheral membrane proteins have been previously reported to associate with the membrane via charged regions^{20–22,27,31}. We speculate that some of these charge-sensitive components in turn initiate downstream events that mediate further loss of multiple anionic lipids in the front regions, further decreasing the membrane surface charge. Such feedback loops would enable small fluctuations to expand into propagating waves and can have outsized phenotypic effects. This architecture would be analogous to the ability of transmembrane potential to regulate key ion channels, which in turn regulate the transmembrane potential during action potential propagation.

The action surface potential hypothesis can explain a series of heretofore puzzling observations. First, as we discussed, a vast number of signal transduction activities undergo a highly coordinated stereotypical transient response. This extraordinary degree of coordination within an extensive series of stepwise interactions could be facilitated if the regulation of key components depended on an organizer located on the inner surface of the membrane, such as the surface charge. Second, cells expend a substantial amount of energy to sustain an asymmetrical distribution of anionic lipids on the inner leaflet of the membrane, which has little apparent structural advantage. Of course, PIP2 serves as a substrate for PLC and PI3K, and PS as a signal for apoptosis. However, we suggest that another, perhaps larger, role of this asymmetrical distribution of charged lipids is to set up the basal state for triggering the action surface potentials, which involve changes in multiple lipids acting in a common direction. Third, the excitable nature of the action surface potentials could underly oscillations for frequency control of gene expression and enable global control over cytoskeletal activities. In the latter case, the lateral propagation of the waves along the cortex in more-or-less circular patterns provides form and dimension to protrusions that enable cells to polarize and migrate, engulf nutrients and divide. Recent reports highlight that travelling waves of cytoskeletal and signalling activities mediate a diverse range of physiological processes in various cells and organisms^{12,66–68,85,94–99}. Our results imply that the action surface potential probably contributes in spatiotemporally orchestrating all these events.

Online content

Any methods, additional references, Nature Research reporting summaries, source data, extended data, supplementary information, acknowledgements, peer review information; details of author contributions and competing interests; and statements of data and code availability are available at <https://doi.org/10.1038/s41556-022-00997-7>.

References

- Saha, S., Nagy, T. L. & Weiner, O. D. Joining forces: crosstalk between biochemical signalling and physical forces orchestrates cellular polarity and dynamics. *Philos. Trans. R. Soc. B* **373**, <https://doi.org/10.1098/rstb.2017.0145> (2018).
- Manning, B. D. & Toker, A. AKT/PKB signaling: navigating the network. *Cell* **169**, 381–405 (2017).
- Devreotes, P. N. et al. Excitable signal transduction networks in directed cell migration. *Annu. Rev. Cell Dev. Biol.* **33**, 103–125 (2017).
- Hoxhaj, G. & Manning, B. D. The PI3K–AKT network at the interface of oncogenic signalling and cancer metabolism. *Nat. Rev. Cancer* **20**, 74–88 (2020).
- Ridley, A. J. et al. Cell migration: integrating signals from front to back. *Science* **302**, 1704–1709 (2003).
- Pal, D. S., Li, X., Banerjee, T., Miao, Y. & Devreotes, P. N. The excitable signal transduction networks: movers and shapers of eukaryotic cell migration. *Int. J. Dev. Biol.* **63**, 407–416 (2019).
- Swaney, K. F., Huang, C. H. & Devreotes, P. N. Eukaryotic chemotaxis: a network of signaling pathways controls motility, directional sensing, and polarity. *Annu. Rev. Biophys.* **39**, 265–289 (2010).
- Shellard, A., Szabo, A., Trepast, X. & Mayor, R. Supracellular contraction at the rear of neural crest cell groups drives collective chemotaxis. *Science* **362**, 339–343 (2018).
- Miao, Y. et al. Altering the threshold of an excitable signal transduction network changes cell migratory modes. *Nat. Cell Biol.* **19**, 329–340 (2017).
- Houk, A. R. et al. Membrane tension maintains cell polarity by confining signals to the leading edge during neutrophil migration. *Cell* **148**, 175–188 (2012).
- Yang, J. M. et al. Integrating chemical and mechanical signals through dynamic coupling between cellular protrusions and pulsed ERK activation. *Nat. Commun.* **9**, 4673 (2018).
- Zhan, H. et al. An excitable Ras/PI3K/ERK signaling network controls migration and oncogenic transformation in epithelial cells. *Dev. Cell* **54**, 608–623 (2020).
- Dai, W. et al. Tissue topography steers migrating *Drosophila* border cells. *Science* **370**, 987–990 (2020).
- Graziano, B. R. et al. Cell confinement reveals a branched-actin independent circuit for neutrophil polarity. *PLoS Biol.* **17**, e3000457 (2019).
- Dang, I. et al. Inhibitory signalling to the Arp2/3 complex steers cell migration. *Nature* **503**, 281–284 (2013).
- O’Neill, P. R. et al. Membrane flow drives an adhesion-independent amoeboid cell migration mode. *Dev. Cell* **46**, 9–22 (2018).
- Lampert, T. J. et al. Shear force-based genetic screen reveals negative regulators of cell adhesion and protrusive activity. *Proc. Natl Acad. Sci. USA* **114**, E7727–E7736 (2017).
- Fort, L. et al. Fam49/CYRI interacts with Rac1 and locally suppresses protrusions. *Nat. Cell Biol.* **20**, 1159–1171 (2018).
- Kholodenko, B. N., Hancock, J. F. & Kolch, W. Signalling ballet in space and time. *Nat. Rev. Mol. Cell Biol.* **11**, 414–426 (2010).
- McLaughlin, S. & Murray, D. Plasma membrane phosphoinositide organization by protein electrostatics. *Nature* **438**, 605–611 (2005).
- Yeung, T. et al. Receptor activation alters inner surface potential during phagocytosis. *Science* **313**, 347–351 (2006).
- Ma, Y., Poole, K., Goyette, J. & Gaus, K. Introducing membrane charge and membrane potential to T cell signaling. *Front. Immunol.* **8**, 1513 (2017).
- Goldenberg, N. M. & Steinberg, B. E. Surface charge: a key determinant of protein localization and function. *Cancer Res.* **70**, 1277–1280 (2010).
- Rickert, P., Weiner, O. D., Wang, F., Bourne, H. R. & Servant, G. Leukocytes navigate by compass: roles of PI3K γ and its lipid products. *Trends Cell Biol.* **10**, 466–473 (2000).
- Parent, C. A. & Devreotes, P. N. A cell’s sense of direction. *Science* **284**, 765–770 (1999).

26. Senju, Y. & Lappalainen, P. Regulation of actin dynamics by PI(4,5)P₂ in cell migration and endocytosis. *Curr. Opin. Cell Biol.* **56**, 7–13 (2019).
27. McLaughlin, S. The electrostatic properties of membranes. *Annu. Rev. Biophys. Biophys. Chem.* **18**, 113–136 (1989).
28. Eisenberg, S. et al. Mapping the electrostatic profile of cellular membranes. *Mol. Biol. Cell* **32**, 301–310 (2020).
29. Murray, D. et al. Electrostatic properties of membranes containing acidic lipids and adsorbed basic peptides: theory and experiment. *Biophys. J.* **77**, 3176–3188 (1999).
30. Aguilera, V. M., Verdia-Baguena, C. & Alcaraz, A. Lipid charge regulation of non-specific biological ion channels. *Phys. Chem. Chem. Phys.* **16**, 3881–3893 (2014).
31. Heo, W. D. et al. PI(3,4,5)P₃ and PI(4,5)P₂ lipids target proteins with polybasic clusters to the plasma membrane. *Science* **314**, 1458–1461 (2006).
32. Alexander, R. T. et al. Membrane surface charge dictates the structure and function of the epithelial Na⁺/H⁺ exchanger. *EMBO J.* **30**, 679–691 (2011).
33. Green, W. N. & Andersen, O. S. Surface charges and ion channel function. *Annu. Rev. Physiol.* **53**, 341–359 (1991).
34. Ma, Y. et al. A FRET sensor enables quantitative measurements of membrane charges in live cells. *Nat. Biotechnol.* **35**, 363–370 (2017).
35. Shi, X. et al. Ca²⁺ regulates T-cell receptor activation by modulating the charge property of lipids. *Nature* **493**, 111–115 (2013).
36. Maxson, M. E. & Grinstein, S. The role of membrane surface charge in phagocytosis. *Adv. Exp. Med. Biol.* **1246**, 43–54 (2020).
37. Li, X. et al. Mutually inhibitory Ras-PI(3,4)P₂ feedback loops mediate cell migration. *Proc. Natl Acad. Sci. USA* **115**, E9125–E9134 (2018).
38. Bagorda, A. & Parent, C. A. Eukaryotic chemotaxis at a glance. *J. Cell Sci.* **121**, 2621–2624 (2008).
39. Gerhardt, M. et al. Actin and PIP₃ waves in giant cells reveal the inherent length scale of an excited state. *J. Cell Sci.* **127**, 4507–4517 (2014).
40. Matsuoka, S. & Ueda, M. Mutual inhibition between PTEN and PIP₃ generates bistability for polarity in motile cells. *Nat. Commun.* **9**, 4481 (2018).
41. Arai, Y. et al. Self-organization of the phosphatidylinositol lipids signaling system for random cell migration. *Proc. Natl Acad. Sci. USA* **107**, 12399–12404 (2010).
42. Masters, T. A., Sheetz, M. P. & Gauthier, N. C. F-actin waves, actin cortex disassembly and focal exocytosis driven by actin-phosphoinositide positive feedback. *Cytoskeleton* **73**, 180–196 (2016).
43. Gerisch, G., Schroth-Diez, B., Muller-Taubenberger, A. & Ecke, M. PIP₃ waves and PTEN dynamics in the emergence of cell polarity. *Biophys. J.* **103**, 1170–1178 (2012).
44. Swaney, K. F., Borleis, J., Iglesias, P. A. & Devreotes, P. N. Novel protein Callipygian defines the back of migrating cells. *Proc. Natl Acad. Sci. USA* **112**, 3845 (2015).
45. Yeung, T. et al. Membrane phosphatidylserine regulates surface charge and protein localization. *Science* **319**, 210–213 (2008).
46. Yeung, T. et al. Contribution of phosphatidylserine to membrane surface charge and protein targeting during phagosome maturation. *J. Cell Biol.* **185**, 917–928 (2009).
47. Zeniou-Meyer, M. et al. Phospholipase D1 production of phosphatidic acid at the plasma membrane promotes exocytosis of large dense-core granules at a late stage. *J. Biol. Chem.* **282**, 21746–21757 (2007).
48. Kassas, N. et al. Genetically encoded probes for phosphatidic acid. *Methods Cell. Biol.* **108**, 445–459 (2012).
49. Dickson, E. J. & Hille, B. Understanding phosphoinositides: rare, dynamic, and essential membrane phospholipids. *Biochem. J.* **476**, 1–23 (2019).
50. Fairn, G. D. et al. An electrostatic switch displaces phosphatidylinositol phosphate kinases from the membrane during phagocytosis. *J. Cell Biol.* **187**, 701–714 (2009).
51. Ingolfsson, H. I. et al. Lipid organization of the plasma membrane. *J. Am. Chem. Soc.* **136**, 14554–14559 (2014).
52. Leventis, R. & Silvius, J. R. Lipid-binding characteristics of the polybasic carboxy-terminal sequence of K-ras4B. *Biochemistry* **37**, 7640–7648 (1998).
53. Fukushima, S., Matsuoka, S. & Ueda, M. Excitable dynamics of Ras triggers spontaneous symmetry breaking of PIP₃ signaling in motile cells. *J. Cell Sci.* **132**, jcs224121 (2019).
54. Jin, T., Zhang, N., Long, Y., Parent, C. A. & Devreotes, P. N. Localization of the G protein β complex in living cells during chemotaxis. *Science* **287**, 1034–1036 (2000).
55. Janetopoulos, C., Ma, L., Devreotes, P. N. & Iglesias, P. A. Chemoattractant-induced phosphatidylinositol 3,4,5-trisphosphate accumulation is spatially amplified and adapts, independent of the actin cytoskeleton. *Proc. Natl Acad. Sci. USA* **101**, 8951–8956 (2004).
56. Miao, Y. et al. Wave patterns organize cellular protrusions and control cortical dynamics. *Mol. Syst. Biol.* **15**, e8585 (2019).
57. Hammond, G. R. et al. PI4P and PI(4,5)P₂ are essential but independent lipid determinants of membrane identity. *Science* **337**, 727–730 (2012).
58. Martin, S. et al. Immunologic stimulation of mast cells leads to the reversible exposure of phosphatidylserine in the absence of apoptosis. *Int. Arch. Allergy Immunol.* **123**, 249–258 (2000).
59. Balasubramanian, K., Mirnikjoo, B. & Schroit, A. J. Regulated externalization of phosphatidylserine at the cell surface: implications for apoptosis. *J. Biol. Chem.* **282**, 18357–18364 (2007).
60. Chung, C. Y., Potikyan, G. & Firtel, R. A. Control of cell polarity and chemotaxis by Akt/PKB and PI3 kinase through the regulation of PAKα. *Mol. Cell* **7**, 937–947 (2001).
61. Meili, R., Ellsworth, C. & Firtel, R. A. A novel Akt/PKB-related kinase is essential for morphogenesis in *Dictyostelium*. *Curr. Biol.* **10**, 708–717 (2000).
62. Kamimura, Y. et al. PIP₃-independent activation of TorC2 and PKB at the cell's leading edge mediates chemotaxis. *Curr. Biol.* **18**, 1034–1043 (2008).
63. van Haastert, P. J., Keizer-Gunnink, I. & Kortholt, A. Essential role of PI3-kinase and phospholipase A2 in *Dictyostelium discoideum* chemotaxis. *J. Cell Biol.* **177**, 809–816 (2007).
64. Hoeller, O. et al. Two distinct functions for PI3-kinases in macropinocytosis. *J. Cell Sci.* **126**, 4296–4307 (2013).
65. Bhattacharya, S. et al. Traveling and standing waves mediate pattern formation in cellular protrusions. *Sci. Adv.* **6**, eaay7682 (2020).
66. Huang, C. H., Tang, M., Shi, C., Iglesias, P. A. & Devreotes, P. N. An excitable signal integrator couples to an idling cytoskeletal oscillator to drive cell migration. *Nat. Cell Biol.* **15**, 1307–1316 (2013).
67. Weiner, O. D., Marganski, W. A., Wu, L. F., Altschuler, S. J. & Kirschner, M. W. An actin-based wave generator organizes cell motility. *PLoS Biol.* **5**, e221 (2007).
68. Bement, W. M. et al. Activator-inhibitor coupling between Rho signalling and actin assembly makes the cell cortex an excitable medium. *Nat. Cell Biol.* **17**, 1471–1483 (2015).
69. Biswas, D., Devreotes, P. N. & Iglesias, P. A. Three-dimensional stochastic simulation of chemoattractant-mediated excitability in cells. *PLoS Comput. Biol.* **17**, e1008803 (2021).

70. Wittmann, T., Dema, A. & van Haren, J. Lights, cytoskeleton, action: optogenetic control of cell dynamics. *Curr. Opin. Cell Biol.* **66**, 1–10 (2020).
71. Tischer, D. & Weiner, O. D. Illuminating cell signalling with optogenetic tools. *Nat. Rev. Mol. Cell Biol.* **15**, 551–558 (2014).
72. Karunarathne, W. K., O'Neill, P. R. & Gautam, N. Subcellular optogenetics—controlling signaling and single-cell behavior. *J. Cell Sci.* **128**, 15–25 (2015).
73. DeRose, R., Miyamoto, T. & Inoue, T. Manipulating signaling at will: chemically-inducible dimerization (CID) techniques resolve problems in cell biology. *Pflug. Arch.* **465**, 409–417 (2013).
74. Inoue, T., Heo, W. D., Grimley, J. S., Wandless, T. J. & Meyer, T. An inducible translocation strategy to rapidly activate and inhibit small GTPase signaling pathways. *Nat. Methods* **2**, 415–418 (2005).
75. Wu, Y. I. et al. A genetically encoded photoactivatable Rac controls the motility of living cells. *Nature* **461**, 104–108 (2009).
76. Karunarathne, W. K., Giri, L., Patel, A. K., Venkatesh, K. V. & Gautam, N. Optical control demonstrates switch-like PIP3 dynamics underlying the initiation of immune cell migration. *Proc. Natl Acad. Sci. USA* **110**, E1575–E1583 (2013).
77. O'Neill, P. R., Kalyanaraman, V. & Gautam, N. Subcellular optogenetic activation of Cdc42 controls local and distal signaling to drive immune cell migration. *Mol. Biol. Cell* **27**, 1442–1450 (2016).
78. Iijima, M. & Devreotes, P. Tumor suppressor PTEN mediates sensing of chemoattractant gradients. *Cell* **109**, 599–610 (2002).
79. Iijima, M., Huang, Y. E., Luo, H. R., Vazquez, F. & Devreotes, P. N. Novel mechanism of PTEN regulation by its phosphatidylinositol 4,5-bisphosphate binding motif is critical for chemotaxis. *J. Biol. Chem.* **279**, 16606–16613 (2004).
80. Wessels, D., Lusche, D. F., Kuhl, S., Heid, P. & Soll, D. R. PTEN plays a role in the suppression of lateral pseudopod formation during *Dictyostelium* motility and chemotaxis. *J. Cell Sci.* **120**, 2517–2531 (2007).
81. Takeda, K., Sasaki, A. T., Ha, H., Seung, H. A. & Firtel, R. A. Role of phosphatidylinositol 3-kinases in chemotaxis in *Dictyostelium*. *J. Biol. Chem.* **282**, 11874–11884 (2007).
82. Cai, H. et al. Ras-mediated activation of the TORC2–PKB pathway is critical for chemotaxis. *J. Cell Biol.* **190**, 233–245 (2010).
83. Shi, C., Huang, C. H., Devreotes, P. N. & Iglesias, P. A. Interaction of motility, directional sensing, and polarity modules recreates the behaviors of chemotaxing cells. *PLoS Comput. Biol.* **9**, e1003122 (2013).
84. O'Neill, P. R. & Gautam, N. Subcellular optogenetic inhibition of G proteins generates signaling gradients and cell migration. *Mol. Biol. Cell* **25**, 2305–2314 (2014).
85. Wu, M. & Liu, J. Mechanobiology in cortical waves and oscillations. *Curr. Opin. Cell Biol.* **68**, 45–54 (2020).
86. Wu, Z., Su, M., Tong, C., Wu, M. & Liu, J. Membrane shape-mediated wave propagation of cortical protein dynamics. *Nat. Commun.* **9**, 136 (2018).
87. Rodriguez-Viciano, P. et al. Phosphatidylinositol-3-OH kinase as a direct target of Ras. *Nature* **370**, 527–532 (1994).
88. Pacold, M. E. et al. Crystal structure and functional analysis of Ras binding to its effector phosphoinositide 3-kinase γ . *Cell* **103**, 931–943 (2000).
89. Myers, M. P. et al. The lipid phosphatase activity of PTEN is critical for its tumor suppressor function. *Proc. Natl Acad. Sci. USA* **95**, 13513–13518 (1998).
90. van den Bogaart, G. et al. Membrane protein sequestering by ionic protein-lipid interactions. *Nature* **479**, 552–555 (2011).
91. Dathe, M. et al. Peptide helicity and membrane surface charge modulate the balance of electrostatic and hydrophobic interactions with lipid bilayers and biological membranes. *Biochemistry* **35**, 12612–12622 (1996).
92. Parthasarathy, R., Cripe, P. A. & Groves, J. T. Electrostatically driven spatial patterns in lipid membrane composition. *Phys. Rev. Lett.* **95**, 048101 (2005).
93. Vazquez, F. et al. Tumor suppressor PTEN acts through dynamic interaction with the plasma membrane. *Proc. Natl Acad. Sci. USA* **103**, 3633–3638 (2006).
94. Inagaki, N. & Katsuno, H. Actin waves: origin of cell polarization and migration? *Trends Cell Biol.* **27**, 515–526 (2017).
95. Cheng, X. & Ferrell, J. E. Apoptosis propagates through the cytoplasm as trigger waves. *Science* **361**, 607–612 (2018).
96. Yang, H. W., Collins, S. R. & Meyer, T. Locally excitable Cdc42 signals steer cells during chemotaxis. *Nat. Cell Biol.* **18**, 191–201 (2016).
97. van Haastert, P. J., Keizer-Gunnink, I. & Kortholt, A. Coupled excitable Ras and F-actin activation mediates spontaneous pseudopod formation and directed cell movement. *Mol. Biol. Cell* **28**, 922–934 (2017).
98. Lange, M., Prassler, J., Ecke, M., Muller-Taubenberger, A. & Gerisch, G. Local Ras activation, PTEN pattern, and global actin flow in the chemotactic responses of oversized cells. *J. Cell Sci.* **129**, 3462–3472 (2016).
99. Xiong, D. et al. Frequency and amplitude control of cortical oscillations by phosphoinositide waves. *Nat. Chem. Biol.* **12**, 159–166 (2016).

Publisher's note Springer Nature remains neutral with regard to jurisdictional claims in published maps and institutional affiliations.

Springer Nature or its licensor holds exclusive rights to this article under a publishing agreement with the author(s) or other rightsholder(s); author self-archiving of the accepted manuscript version of this article is solely governed by the terms of such publishing agreement and applicable law.

© The Author(s), under exclusive licence to Springer Nature Limited 2022

¹Department of Cell Biology and Center for Cell Dynamics, School of Medicine, Johns Hopkins University, Baltimore, MD, USA. ²Department of Chemical and Biomolecular Engineering, Whiting School of Engineering, Johns Hopkins University, Baltimore, MD, USA. ³Department of Electrical and Computer Engineering, Whiting School of Engineering, Johns Hopkins University, Baltimore, MD, USA. ⁴Department of Biological Chemistry, School of Medicine, Johns Hopkins University, Baltimore, MD, USA. ⁵These authors contributed equally: Debojyoti Biswas, Dhiman Sankar Pal. ✉ e-mail: pnd@jhmi.edu

Methods

Cell culture

Wild-type *Dictyostelium discoideum* cells of the axenic strain AX2 were cultured in HL-5 medium at 22 °C. Hygromycin (50 µg ml⁻¹) and/or G418 (30 µg ml⁻¹) were added to the medium to maintain cell lines expressing different constructs. *PI3KI*^{-/-} and *PTEN*^{-/-} *Dictyostelium* cells were cultured as the AX2 cells, whereas heat-killed *Klebsiella aerogenes* were added to the culture medium to culture *PKBA*⁻/*PKBRI*⁻ *Dictyostelium* cells. Cells were usually maintained in Petri dishes and transferred to a shaking culture around 2–4 d before electrofusion or differentiation experiments. *PTEN*^{-/-} *Dictyostelium* cells were always cultured in Petri dishes. All of the experiments were performed within 2 months of thawing the cells from frozen stocks.

RAW 264.7 macrophage-like cells were obtained from the N. Gautam laboratory (Washington University School of Medicine in St. Louis) and mammary epithelial MCF10A cells were obtained from the M. Iijima laboratory (Johns Hopkins University School of Medicine). RAW 264.7 cells were cultured in Dulbecco's modified Eagle's medium (DMEM) containing 4,500 mg l⁻¹ glucose, l-glutamine, sodium pyruvate and sodium bicarbonate (Sigma-Aldrich, D6429), supplemented with 10% heat-inactivated fetal bovine serum (ThermoFisher Scientific, 16140071) and 1% penicillin–streptomycin (ThermoFisher Scientific, 15140122). MCF10A cells were cultured in DMEM/F-12 medium with GlutaMAX (ThermoFisher Scientific, 10565042) supplemented with 5% heat-inactivated horse serum (ThermoFisher Scientific, 26050088), 1% penicillin–streptomycin, 20 ng ml⁻¹ EGF (Sigma-Aldrich, E9644), 100 ng ml⁻¹ cholera toxin, 0.5 mg ml⁻¹ hydrocortisone and 10 µg ml⁻¹ insulin. All cells were subcultured every 2–6 d using cell lineage-specific techniques to maintain a healthy confluency. All experiments were performed using cells with a low passage number. All mammalian cells were maintained under humidified conditions at 37 °C and 5% CO₂.

DNA constructs

All sensors and actuators were usually codon-optimized if used for heterologous expression. R(+8)-Pre was obtained from the C-terminal tail of KRas4b; all the serines and threonines were mutated to alanine to prevent phosphorylation and all the lysines were mutated to arginines to avoid ubiquitination²¹. In R(+7)-Pre, R(+4)-Pre and R(+2)-Pre, the arginines were sequentially mutated to glutamines to reduce the positive charge of the sensor. cARI is a *Dictyostelium* protein that works as a GPCR. Palm/Pre is the C-terminal tail of HRas. PM-LYN is the first 11 amino acids of the human tyrosine-protein kinase LYN. In PTEN₁₋₁₈-CAAX, a CAAX motif was added to the first 18 amino acids of PTEN. RacG_{CT} is the C-terminal tail of RacG, which we identified when we entered the KRas4b tail as a query sequence in NCBI Protein BLAST (blastp), with organism *Dictyostelium* specified in the search set. The optogenetic actuator Opto-ACTU⁺, which has a net charge +16, was designed by removing the CAAX tail from R(+8)-Pre (so that it becomes cytosolic) and making a dimer of it joined by a linker of three glycines. The optogenetic actuator Opto-ACTU⁻, which has a net charge -14, was designed using the C-terminal polyanionic tail sequence of the mouse protein Rad17.

All surface-charge sensors and actuators—that is GFP-R(+8)-Pre, GFP-R(+7)-Pre, GFP-R(+4)-Pre, GFP-R(+2)-Pre, GFP-Palm/Pre, GFP-PTEN₁₋₁₈-CAAX, GFP-RacG_{CT}, Opto-ACTU⁺ and Opto-ACTU⁻—were generated by annealing the appropriate synthetic oligonucleotides, followed by restriction enzyme-mediated digestion and subcloning into the appropriate *Dictyostelium* or mammalian vectors. All other constructs were made by PCR amplification, followed by standard restriction enzyme cloning or using a site-directed mutagenesis kit (QuickChange II; Agilent Technologies, 200523). All oligonucleotides were obtained from Sigma-Aldrich. All sequences were verified by diagnostic restriction digest and standard Sanger sequencing (JHMI Synthesis & Sequencing Facility).

The following plasmid constructs were made in this study. A selection will be deposited on Addgene or dictyBase^{100,101} and the rest will be available from the authors on direct request: (1) GFP-R(+8)-Pre (pDM358), (2) GFP-R(+8)-Pre (pDEXG), (3) GFP-R(+7)-Pre (pDEXG), (4) GFP-R(+4)-Pre (pDEXG), (5) GFP-R(+2)-Pre (pDEXG), (6) GFP-PTEN₁₋₁₈-CAAX (pDEXG), (7) GFP-RacG_{CT} (pDEXG), (8) GFP-LactC2 (pTX-GFP), (9) GFP-Spo20 (pDEXG), (10) Opto-ACTU⁺ (pCV5), (11) Opto-CTRL (pCV5), (12) cARI-CIBN (pDM358), (13) N150_{PKBRI}-CIBN (pDM358), (14) Opto-ACTU⁻ (pmCherryN1) and (15) LimE_{Δcoil}-Halo (pCV5).

GFP-R(+8)-Pre (mammalian) was from S. Grinstein (Addgene, plasmid 17274), GFP-LactC2 (mammalian) was from S. Grinstein (Addgene, plasmid 22852), GFP-Spo20—originally made by Vitale et al.⁴⁸—was a gift from G. Du (McGovern Medical School, UTHealth), mPlum-LimE_{Δcoil} was from A. Müller-Taubenberger (LMU Munich), pCRY2PHR-mCherryN1 (that is, mammalian Opto-CTRL) was from C. Tucker (Addgene, plasmid 26866), CIBN-CAAX was from P. De Camilli and O. Idevall-Hagren (Addgene, plasmid 79574), Lifeact-mVenus was from J. Zhang (Addgene, plasmid 87613), ERK-KTR-irFP713 was from J. Toettcher (Addgene, plasmid 111510), Lyn11-FRB-CFP (Addgene, plasmid 38003) and pseudojanin (Addgene, plasmid 37999) were from R. Irvine, and GFP-OSH2-2xPH (Addgene, plasmid 161987) as well as PH-PLCD1-GFP (Addgene, plasmid 51407) were from T. Balla.

The remaining plasmids used in this study were available in the Devreotes laboratory.

Transfection

Dictyostelium AX2 cells were transfected using a standard electroporation protocol. Briefly, for each transfection, 1 × 10⁷ cells were pelleted, washed twice with ice-cold H-50 buffer (20 mM HEPES, 50 mM KCl, 10 mM NaCl, 1 mM MgSO₄, 5 mM NaHCO₃, 1 mM NaH₂PO₄, pH adjusted to 7.0) and subsequently resuspended in 100 µl ice-cold H-50 buffer. Around 1–5 µg of total DNA was mixed with the cell suspension, which was then transferred to an ice-cold 0.1-cm-gap cuvette (Bio-Rad, 1652089) for two rounds of electroporation at 850 V and 25 µF with an interval of 5 s (Bio-Rad Gene Pulser Xcell Electroporation Systems). After a 5-min incubation on ice, the electroporated cells were transferred to a 10-cm Petri dish containing HL-5 medium supplemented with heat-killed *K. aerogenes* bacteria. The cells were selected by the addition of hygromycin B (50 µg ml⁻¹) and/or G418 (20–30 µg ml⁻¹) after 1–2 d as per the antibiotic resistance of the vectors. For optogenetics and chemically induced dimerization experiments where three different protein co-expressions were necessary, two different pCV5 vectors and one pDM358 vector were used and cells were selected against both drugs.

RAW 264.7 cells were transfected by nucleofection in an Amaxa Nucleofector II device using Amaxa Cell line kit V (Lonza, VACA-1003) following a pre-existing protocol¹⁰². For each transfection, 3 × 10⁶ cells were harvested, resuspended in 100 µl supplemented Nucleofector Solution V. A total of 4–6 µg of DNA mixture was added and immediately transferred to a Lonza cuvette for electroporation using the program setting D-032. Pre-warmed pH-adjusted culture medium (500 µl) was added to the electroporated cells in the cuvette. The cell suspension was then transferred to a 1.5 ml vial and incubated at 37 °C and 5% CO₂ for 10 min. Next, 50–100 µl solution containing cells was transferred to a coverslip chamber and allowed to adhere for 1 h. Finally, approximately 400 µl of pre-warmed pH-adjusted culture medium was added to each chamber and the cells were further incubated for 4–6 h before imaging.

MCF10A cells were transiently transfected using Lipofectamine 3000 transfection reagent (ThermoFisher Scientific, L3000001) as per the manufacturer's protocol. Briefly, approximately 0.8 µg DNA was mixed in 160 µl of serum-free Opti-MEM medium (ThermoFisher Scientific, 31985062) containing 3 µl Lipofectamine 3000 reagent and incubated for 5–7 min at room temperature to allow formation of DNA–lipid complexes. Following incubation, the DNA–lipid complex

was added to 2×10^5 MCF10A cells plated on a two-well glass chamber. The cells were incubated at 37 °C with 5% CO₂ for 5 h, after which the DNA–lipid complex was removed, and the cells were thoroughly washed and incubated for a further 12–18 h before imaging.

Drugs and reagents

Annexin V–Alexa Fluor 488 conjugate was obtained from ThermoFisher Scientific (Invitrogen, A13201) and stored in 4 °C. Latrunculin A (Enzo Life Sciences, BML-T119-0100) was dissolved in dimethylsulfoxide (DMSO) to make a stock solution of 5 mM. Caffeine (Sigma-Aldrich, C0750) was dissolved in ddH₂O to make a stock solution of 80 mM. Rapamycin (Sigma-Aldrich, 553210) was dissolved in DMSO to prepare a 10 mM stock solution. cAMP (Sigma-Aldrich, A6885) was dissolved in ddH₂O to make a stock solution of 10 mM. Janelia Fluor 646 HaloTag (Promega Corporation, GA1120) was dissolved in DMSO to prepare a 200 μM stock solution, which was stored in 4 °C and diluted 1,000× during the experiment. The C5a-receptor agonist FKP-(D-Cha)-Cha-r (Anaspec, 65121) was dissolved in 1×PBS to make a 2.5 mM stock solution. Anti-BSA was obtained from Sigma-Aldrich (SAB4200688). A stock solution of EGF (Sigma-Aldrich, E9644) was prepared by dissolving it in 10 mM acetic acid to a final concentration of 1 mg ml⁻¹. Hydrocortisone (Sigma-Aldrich, H0888) was dissolved in 200-proof ethanol to make a 1 mg ml⁻¹ stock. Insulin (Sigma-Aldrich, I1882) was resuspended in sterile ddH₂O (containing 1% glacial acetic acid) to make a 10 mg ml⁻¹ stock solution. Cholera toxin (Sigma-Aldrich, C-8052) was dissolved in sterile ddH₂O to make a 1 mg ml⁻¹ stock solution and stored at 4 °C. LY294002 was obtained from ThermoFisher Scientific (Invitrogen, PHZ1144) and dissolved in DMSO to make a 40 mM solution. PP242 (Sigma-Aldrich, 475988) was dissolved in DMSO to prepare a 20 mM stock solution. Unless otherwise mentioned, all solutions were stored as small aliquots at –20 °C.

Microscopy and live-cell imaging

Unless otherwise specified, all experiments were performed inside a heated (37 °C) chamber with 5% CO₂ supply (for mammalian-cell imaging) or on a 22 °C stage (for *Dictyostelium* imaging). All time-lapse live-cell images were acquired using one of the following four microscopes: (1) Zeiss LSM780-FCS single-point, laser scanning confocal microscope (Zeiss Axio Observer with 780-Quasar; 34-channel spectral, high-sensitivity gallium arsenide phosphide detectors), (2) Zeiss LSM880-Airyscan FAST super-resolution single-point confocal microscope (Zeiss Axio Observer with 880-Quasar; 34-channel spectral, high-sensitivity gallium arsenide phosphide detectors), (3) Zeiss LSM800 GaAsP single-point laser scanning confocal microscope with wide-field camera and (4) Nikon Eclipse Ti-E dSTROM total internal reflection fluorescence (TIRF) microscope (Photometrics Evolve EMCCD camera).

In the Zeiss 780 and 800 microscopes, 488 nm (argon laser) excitation was used for GFP; 561 nm (solid-state) excitation was used for RFP, mCherry and mPlum; and 633 nm (diode laser) excitation was used for iRFP713 and Janelia Fluor 646 HaloTag. In the Zeiss 880 microscope, 488 nm (argon laser) excitation was used for GFP, 514 nm (argon laser) excitation was used for YFP and mVenus, 594 nm (HeNe laser) excitation was used for mCherry and 633 nm (diode laser) excitation was used for iRFP713. In the Nikon TIRF microscope, 488 nm (argon laser) excitation was used for GFP and 561 nm (0.5 W fibre laser) excitation was used for mCherry and RFP. In the Zeiss 780, 800 and 880 microscopes, a ×40/1.30 Plan-Neofluar oil objective (with the appropriate digital zoom) was used and in the Nikon TIRF microscope, a ×100/1.4 Plan-Apo oil objective was used. Both the Zeiss 780 and 880 confocal microscopes were operated using the ZEN black software, the Zeiss 800 confocal microscope was operated using the ZEN blue software, whereas the Nikon TIRF was controlled using Nikon NIS-Elements. To visualize cortical/ventral waves in *Dictyostelium* and RAW 264.7 cells, either the TIRF microscope was used or confocal microscopes were focused on

the very bottom of the cell to capture the substrate-attached ventral surface of the cell.

Cell differentiation

For *Dictyostelium* cell development, 8×10^7 cells in the exponential growth phase were collected from suspension culture and pelleted as previously described¹⁰³. After two washes with Development buffer (DB; 5 mM Na₂HPO₄ and 5 mM KH₂PO₄ supplemented with 2 mM MgSO₄ and 0.2 mM CaCl₂), the cells were resuspended in 4 ml DB and shaken at 110 r.p.m. for 1 h. The cells were then pulsed with 50–100 nM cAMP (5-s pulse every 6 min) using a time-controlled peristaltic pump for 5–6 h with continual shaking. This allowed the cells to become developed and polarized. After development, $2\text{--}5 \times 10^4$ cells were transferred from the shaker to an eight-well coverslip chamber, resuspended thoroughly in 450 μl DB and incubated for 20–30 min before starting the image acquisition.

Frustrated phagocytosis and osmotic shock

To visualize ventral waves in RAW 264.7 macrophages, we slightly modified a pre-existing protocol⁴². Briefly, Nunc Lab-Tek eight-well coverslip chambers were pre-washed with 30% nitric acid, coated with 1 mg ml⁻¹ BSA for 3 h, washed with PBS and finally incubated with 5 μg ml⁻¹ anti-BSA (1:200 dilution) for 2 h. The chambers were finally washed twice with PBS to remove excess antibodies. Before imaging, transfected RAW 264.7 cells were starved in suspension in 1×Ringer's buffer (150 mM NaCl, 5 mM KCl, 1 mM CaCl₂, 1 mM MgCl₂, 20 mM HEPES and 2 g l⁻¹ glucose, pH 7.4) for 30 min. Next, these cells were introduced to the opsonized chambers and allowed to spread on the antibody-coated surface for 5–10 min, and then hypotonic shock was applied using 0.5×Ringer's solution.

Electrofusion

Dictyostelium cells in the exponential growth phase were collected from suspension culture, washed and resuspended in 10 ml SB buffer (17 mM Soerensen buffer containing 15 mM KH₂PO₄ and 2 mM Na₂HPO₄, pH 6.0) at a density of 1.5×10^7 cells ml⁻¹, as previously described^{39,56}. The cells were rolled gently in a conical tube for 30–40 min to promote the formation of visible clusters. The rolled cells (800 μl) were transferred to a 4-mm-gap Bio-Rad electroporation cuvette using pipette tips with cut-off edges. The electroporation was performed once at 1 kV and 3 μF, followed by electroporation at 1 kV and 1 μF twice more (with a 3-s gap between the two pulses) to facilitate membrane hemifusion. The cells (35 μl) were transferred from the cuvette to a Nunc Lab-Tek eight-well chamber, incubated for an additional 5 min and then fresh SB buffer supplemented with 2 mM CaCl₂ and 2 mM MgCl₂ was gently added to these cells. The cells were incubated at 22 °C for the next 1–1.5 h for recovery before imaging.

Annexin V-binding assay

Dictyostelium cells in the growth phase were transferred to an eight-well Nunc Lab-Tek coverslip chamber and allowed to adhere for 10–15 min. The HL-5 medium was removed and 450 μl DB buffer was added to the cells. The cells were incubated at 22 °C for 60–120 min, after which the DB buffer was exchanged with DB buffer containing excess calcium (CaCl₂ at a final concentration of 2.5 mM) and incubated for 30 min. The coverslip chambers were transferred to an ice bath (to slow down the protrusion formation and withdrawal frequency) and the remainder of the procedure was performed on ice. Next, 10 μl of the annexin V–Alexa Fluor 488 conjugate was added to each well and allowed to bind for 45–60 s. The medium (containing annexin V–Alexa Fluor 488 conjugate) was aspirated and quickly washed twice using DB with excess calcium buffer to get rid of all unbound annexin V. The cells were then fixed without permeabilization using 2% paraformaldehyde and 0.25% glutaraldehyde in HL-5 (with 2.5 mM Ca²⁺) for 15 min, washed twice and finally put under DB with excess calcium for imaging.

Gradient stimulation assay

The gradient stimulation assay by cAMP-filled needle was performed as per the established protocol^{99,103,104}. *Dictyostelium* cells coexpressing PH_{crac}-mCherry and GFP-R(+8)-Pre were differentiated (as described in the 'Cell differentiation' section) for 5.5–6.5 h and then placed under a cAMP gradient. The cells were pre-treated with latrunculin A to inhibit cytoskeletal activities. A 10 μM cAMP-filled micropipette (Femtotips, Eppendorf) connected to a FemtoJet microinjector (Eppendorf) was used to provide the gradient stimulation. The microinjector was employed in continuous injection mode with a compensation pressure of 70 hPa. Stimulation was induced by suddenly bringing the micropipette (using the micromanipulator) close to the *x, y, z* coordinate of the cell that was being imaged and putting it at one side of that cell.

Chemically induced dimerization

The plasmids and experimental details of the chemically induced dimerization system have mostly been previously described^{9,56}. Here, to generate Fig. 3a–e and Extended Data Fig. 6a–c, the two following combinations were used to express the systems: (1) cARI-FKBP-FKBP (pCV5) as the membrane anchor, mCherry-FRB-Inp54p (pCV5) as the recruitee and GFP-R(+8)-Pre (pDM358) as the readout; and (2) cARI-FKBP-FKBP (pDM358) as the membrane anchor, mCherry-FRB-Inp54p (pCV5) as the recruitee and PH_{PLCδ}-YFP (pCV5) as the readout. *Dictyostelium* cells in the growth phase were transferred to an eight-well coverslip chamber and incubated for 10–15 min to allow them to adhere well. The HL-5 medium was then replaced with 450 μl DB buffer. Image acquisition was started 15–20 min after the medium change. After imaging a certain number of frames, rapamycin was added gently to the chamber (to a final concentration of 5 μM) during image acquisition to facilitate the recruitment of Inp54p to the plasma membrane. For Fig. 3e, we first ensured that Inp54p had been recruited to the membrane by looking at a few confocal slices at the middle of the cell and then focused to the substrate-attached surface to visualize waves.

To perform chemically induced dimerization-mediated recruitment in RAW 264.7 macrophages, pseudojanin, Lyn11-FRB-CFP and GFP-R(+8)-Pre/GFP-OSH2-2×PH/GFP-PH-PLCδ were nucleofected (as described earlier). After 4–6 h of nucleofection, the culture medium was replaced with 450 μl fresh warm Hank's balanced salt solution (HBSS buffer) containing 1 g l⁻¹ glucose and the cells were incubated for another 0.5–1 h before imaging. After recording a certain number of frames for 2–5 min, rapamycin was introduced during imaging (as described earlier).

Optogenetic regulation of cell migration

To analyse the effect of lowered surface charge on the polarity and migration pattern of cells, *Dictyostelium* cells were selected against both hygromycin and G418 to co-express LimE_{Δcoil}-Halo (pCV5)/RBD-GFP(CV5)/PH_{crac}-YFP(CV5) and cARI-CIBN (pDM358), along with Opto-ACTU⁺ (pCV5) or Opto-CTRL (pCV5). The cells were properly developed as described earlier. After 6–7 h of development, around 2–5 × 10⁴ cells were collected from the shaker and transferred to an eight-well coverslip chamber. The cells were thoroughly resuspended in 450 μl DB buffer and incubated for approximately 20 min before initiating image acquisition. For the experiments presented in Fig. 6e,f and Extended Data Fig. 9d–m, the appropriate developed *Dictyostelium* cells were incubated with either 40 μM LY294002 or 20 μM PP242, or both, for >45 min in DB buffer before image acquisition was started. For global recruitment experiments, after imaging ≥320 s, the 488 nm laser was turned on globally to initiate recruitment and intermittently turned on at a lower intensity during image acquisition (usually for approximately 970 ms after each 8 s) to keep Opto-ACTU⁺ or Opto-CTRL on the membrane throughout the imaging. For spatially confined optical recruitment, a region of interest was drawn and that particular area was illuminated with a 488-nm laser in multiple iterations.

For the surface-charge elevation experiments, RAW 264.7 macrophage cells coexpressing Lifeact-mVenus, CIBN-CAAX and Opto-ACTU⁺ or Opto-CTRL were used. After 4–6 h of nucleofection, the medium was aspirated from the chambers, and the cells were placed in 450 μl of fresh warm HBSS buffer containing 1 g l⁻¹ glucose and incubated for another 0.5–1 h before image acquisition. During imaging, Opto-ACTU⁺ or Opto-CTRL were selectively recruited using a 488-nm laser (as described above), the C5a-receptor agonist FKP-(D-Cha)-Cha-r was then added (diluted in HBSS; final concentration of 10 μM) and image acquisition was continued.

Optogenetic deactivation of ERK

KTR sensors enable the conversion of specific kinase activities into a nucleocytoplasmic shuttling equilibrium for convenient visualization and quantification^{11,105}. Basically, the ERK-KTR sensor becomes cytosolic to nuclear following the deactivation of ERK. To analyse the effect of optogenetic perturbation of the inner-membrane surface charge, MCF10A cells were transfected with ERK-KTR-iRFP713 (as the readout) and CIBN-CAAX (as the membrane anchor) along with Opto-ACTU⁺ or Opto-CTRL (as the recruitee). The transfected cells were incubated overnight in complete culture medium containing 5% horse serum, 10 μg ml⁻¹ insulin and 20 ng ml⁻¹ EGF, which facilitated the activation of ERK. Imaging was performed in the same medium. After 25 min of image acquisition, a 488-nm laser was globally switched on to facilitate recruitment and intermittently turned on during image acquisition to keep Opto-ACTU⁺ or Opto-CTRL on the membrane throughout the imaging. The ERK-KTR localization profile was used to quantitate ERK activity throughout the time period of the experiment.

Image analysis

Image analysis was performed using MATLAB 2019a (MathWorks) and Fiji/ImageJ 1.52i (NIH). The results were plotted using MATLAB 2019a, OriginPro 9.0 (OriginLab) or GraphPad Prism 8 (GraphPad Software).

Co-localization study. Image analysis for the co-localization study was performed with custom codes written in MATLAB 2019a. As the pre-processing steps, the background subtraction and the Gaussian/top-hat filtering were applied to all the images. The cell area from the background and the bright patches of the protein of interest from the cell area were segmented using the thresholding method.

To quantify the extent of co-localization between two proteins of interest in a cell—proteins A and B—the following CPs were computed:

1. Prob(A_{high}|B_{high}): the probability of finding 'high localization' of protein A in the regions of high localization of protein B.
2. Prob(B_{high}|A_{high}): the probability of finding high localization of protein B in the regions of high localization of protein A.
3. Prob(A_{high}|B_{low}): the probability of finding high localization of protein A in the regions of 'low localization' of protein B.
4. Prob(A_{low}|B_{high}): the probability of finding low localization of protein A in the regions of high localization of protein B.
5. Prob(B_{high}|A_{low}): the probability of finding high localization of protein B in the regions of low localization of protein A.
6. Prob(B_{low}|A_{high}): the probability of finding low localization of protein B in the regions of high localization of protein A.

High and the low localization of a protein is decided by the threshold values assumed in the segmentation step. If both the proteins A and B were co-localized in a cell, then the following inequalities would hold true:

$$\text{Prob}(A_{\text{high}}|B_{\text{high}}) > \text{Prob}(A_{\text{high}}|B_{\text{low}}), \quad (1)$$

$$\text{Prob}(A_{\text{high}}|B_{\text{high}}) > \text{Prob}(A_{\text{low}}|B_{\text{high}}), \quad (2)$$

$$\text{Prob}(B_{\text{high}}|A_{\text{high}}) > \text{Prob}(B_{\text{high}}|A_{\text{low}}), \quad (3)$$

$$\text{Prob}(B_{\text{high}}|A_{\text{high}}) > \text{Prob}(B_{\text{low}}|A_{\text{high}}). \quad (4)$$

The inequality sign would be preserved under the change of ordering. The sign reverses if the proteins do not co-localize. In case of the co-localization, the ratio of these CPs (from equations (1)–(4)) will be greater than one, whereas it will be less than one for the cases of complementary localization. Logarithmic transformation of these ratios further differentiates these two cases, leading to positive and negative values, respectively. For concise representation of the data, we computed the following average of the four ratios of CPs for each image frame as follows and named it the CP index:

$$\text{CP index}_{A-B,i} = \frac{1}{4} \left[\log_{10} \left(\frac{\text{Prob}(A_{\text{high}}|B_{\text{high}})}{\text{Prob}(A_{\text{high}}|B_{\text{low}})} \right) + \log_{10} \left(\frac{\text{Prob}(A_{\text{low}}|B_{\text{high}})}{\text{Prob}(A_{\text{low}}|B_{\text{low}})} \right) \right. \\ \left. + \log_{10} \left(\frac{\text{Prob}(B_{\text{high}}|A_{\text{high}})}{\text{Prob}(B_{\text{high}}|A_{\text{low}})} \right) + \log_{10} \left(\frac{\text{Prob}(B_{\text{low}}|A_{\text{high}})}{\text{Prob}(B_{\text{low}}|A_{\text{low}})} \right) \right].$$

For the box-and-whisker plot representations, we averaged the CP index over n frames analysed for every cell image (Avg. CP index) as follows:

$$\text{Avg. CP index}_{A-B} = \frac{1}{n_f} \sum_{i=1}^{n_f} \text{CP index}_{A-B,i}$$

where n_f (≥ 20) is the total number of frames analysed for a sample.

Kymographs. For the membrane kymographs, the cells were segmented against the background following standard image-processing steps with custom code written in MATLAB 2019b. The kymographs were created from the segmented cells as previously described, where consecutive lines over time were aligned by minimizing the sum of the Euclidean distances between the coordinates in two consecutive frames using a custom-written MATLAB function⁶⁶. A linear colourmap was used for the normalized intensities in the kymographs. For grayscale kymographs, black indicates the lowest intensity and white the highest; in coloured kymographs, the lowest intensity is indicated by blue and the highest by yellow.

Line kymographs that accompanied ventral waves were generated in Fiji/ImageJ by drawing a thick line with a line width of 8–12 pixels and processing the entire stack in the ‘KymographBuilder’ plugin.

Line-scan intensity profile. Line scans were performed in Fiji/ImageJ (NIH) by drawing a straight-line segment (using line tool) inside the cells with a line width of 8–12 pixels to obtain an average intensity value. The intensity values along that particular line were obtained in the green and red channels using the ‘Plot Profile’ option. The values were saved and normalized in OriginPro 9.0 (OriginLab). The intensity profiles were graphed and finally smoothed using the Savitzky–Golay or adjacent-averaging method, using proper boundary conditions. The plots were then normalized by dividing by the maximum value. For a particular line scan, the green and red profiles were smoothed and processed using the exact same parameters to maintain consistency.

Time-series plot of the membrane/cytosol ratio. To make the plots in Fig. 3c and Extended Data Fig. 6a, cells were first segmented into membrane and cytosolic masks following standard image-processing steps using custom code written in MATLAB 2019b. The average intensities from the channels were computed for both the masks. The computed intensities were later corrected for the photobleaching effect by dividing the values by an exponential fit to the temporal profiles of the respective normalized average intensities in the cell. Finally, we computed the ratios of the corrected average intensities for different

channels. For the plotting of the temporal profiles of the red-channel data, we normalized the pre-recruitment average profiles to unity, whereas for the green channel, the normalization was done using the respective steady-state value.

Cell tracking and migration analysis. Using the ‘Threshold’ option of Fiji/ImageJ, the image stack was first thresholded properly so that the generated binary image covered all of the pixels of the cells. The range was not reset and the ‘Calculate threshold for each image’ option was unchecked. Subsequently, using the ‘Analysed Particles’ option, a size-based thresholding was applied (to exclude non-cell particles) and cell masks were generated. Next, the ‘Fill holes’, ‘Erode’ and ‘Dilate’ options were applied, sequentially and judiciously, to obtain the proper binarized mask for cells. To generate the migrating cell outlines in Fig. 5g and Extended Data Fig. 9i, the ‘Outline’ command was operated on binarized cells and finally ‘Temporal-Color Code’ was used. For the other plots in Fig. 5 and Extended Data Fig. 9, the ‘Shape descriptors’ and ‘Centroid’ options (inside ‘Set Measurement’) were used with the ‘Analysed Particles’ command to obtain the values of centroid coordinates and circularity values (circularity = $4\pi \times \text{area} / \text{perimeter}^2$). For the centroid, the starting point was set to the origin for each track by applying $x'_i = (x_i - x_0)$ and $y'_i = (y_i - y_0)$ for $i = 0$ to $(n - 1)$. The new translated coordinates were plotted to generate the tracks. The same increment colourmap (OriginPro) was used in the before-recruitment and after-recruitment tracks to enable pairwise comparison in Fig. 5d and Extended Data Fig. 9c,h. For velocity, displacement between each two frames was computed using $d = \sqrt{(x_{i+1} - x_i)^2 + (y_{i+1} - y_i)^2}$, which was divided by the time interval to compute the speed. These speeds were time-averaged to generate each data point in the migration-speed boxplots.

Global protrusion-formation analysis. The frequency of new protrusion formation following global recruitment of Opto-ACTU⁺ or Opto-CTRL was computed in Fiji/ImageJ. In the stack of the binarized cell masks (binarization was performed as per the method described in the ‘Cell tracking and migration analysis’ section), the ‘Stack Difference’ command of ‘Multi Kymograph’ was applied. The stack was inverted and a size-based thresholding was performed. If required, the resulting stack was processed further using the ‘Despeckle’ command and then the protrusions were manually counted. Protrusions were counted for the same frames for which the migration speed was quantified.

Selective protrusion-formation analysis. To perform the selective protrusion-formation analysis following confined recruitment of Opto-ACTU⁺, Opto-ACTU⁻ or Opto-CTRL, we segmented the recruitment area on the membrane with proper threshold. We then marked the area using the segmented line tool. Using a custom-written ImageJ Macro, the ‘Fit spline’ and ‘Straighten’ commands were sequentially operated. The macro was then used to find and mark the midpoint. The centroid of the cell was found and marked using another macro. Using the angle tool, considering the centroid as the vertex, the angles between protrusions and the midpoint of the recruitment areas were obtained. The values were imported to MATLAB and plotted using the ‘polarhistogram’ command. Sturges’ formula was used to determine the minimum number of bins.

KTR-translocation analysis. The nucleus-to-cytosol ratio of ERK–KTR over time was computed to quantitate the extent of ERK deactivation following Opto-ACTU⁻ or Opto-CTRL recruitment. The cells were first segmented in Fiji/ImageJ (as described earlier in the ‘Cell tracking and migration analysis’ section). Using the ‘Analyse Particles’ option, the intensities of the whole cell were obtained. The nucleus intensities were obtained manually by selecting the nucleus from the phase channels of the stack. The cytosolic intensities were found by subtracting the nuclear intensity from the whole-cell intensity. After the

ratios were determined, a conditional formatting rule was applied in Microsoft Excel to generate heatmaps in Extended Data Fig. 10g,h. The mean \pm s.e.m. of these ratios were calculated and plotted in Fig. 8i.

Statistics and reproducibility

The statistical analyses were performed using MATLAB 2019a and GraphPad Prism 8. Time-series data are shown as the mean \pm s.e.m. or mean \pm s.d., as indicated. All boxplots were graphed following Tukey's convention. Statistical significance and *P* values were determined by paired or unpaired two-tailed non-parametric tests, as indicated in the figure captions. Sample sizes were chosen empirically as per the standard custom followed in the field and similar sample sizes were used for the experiment and control groups. For the chemically induced dimerization and optogenetics experiments, data in either the control or experiment group were excluded when there was no recruitment because it essentially implies the absence of expression of the untagged membrane anchor in that particular cell. No other data were excluded from the study. All reported findings were reliably reproduced using at least three biological replicates. To make any experiment or control group cell lines, cells were collected randomly from the parental cell lines in culture. The time at which any drug treatment and/or imaging experiment was performed (with any custom cell line) was chosen randomly. The investigators were not blinded to allocation during experiments and outcome assessment. The following convention was followed to show *P* values: NS, not significant ($P > 0.05$); * $P \leq 0.05$; ** $P \leq 0.01$; *** $P \leq 0.001$ and **** $P \leq 0.0001$.

Reporting summary

Further information on research design is available in the Nature Research Reporting Summary linked to this article.

Data availability

Source data are provided with this paper. All other data supporting the findings of this study are available from the corresponding author on reasonable request.

Code availability

Computational simulation codes are available on GitHub: <https://github.com/tatsatb/Simulation-of-Membrane-Surface-Charge-Perturbation>. Any additional information will be available from the corresponding author on reasonable request.

References

100. Kreppl, L. et al. dictyBase: a new *Dictyostelium discoideum* genome database. *Nucleic Acids Res.* **32**, D332–D333 (2004).
101. Fey, P., Dodson, R. J., Basu, S. & Chisholm, R. L. One stop shop for everything *Dictyostelium*: dictyBase and the Dicty Stock Center in 2012. *Methods Mol. Biol.* **983**, 59–92 (2013).
102. Meshik, X., O'Neill, P. R. & Gautam, N. Optogenetic control of cell migration. *Methods Mol. Biol.* **1749**, 313–324 (2018).
103. Kamimura, Y., Tang, M. & Devreotes, P. Assays for chemotaxis and chemoattractant-stimulated TorC2 activation and PKB substrate phosphorylation in *Dictyostelium*. *Methods Mol. Biol.* **571**, 255–270 (2009).
104. Cai, H., Huang, C. H., Devreotes, P. N. & Iijima, M. Analysis of chemotaxis in *Dictyostelium*. *Methods Mol. Biol.* **757**, 451–468 (2012).

105. de la Cova, C., Townley, R., Regot, S. & Greenwald, I. A real-time biosensor for ERK activity reveals signaling dynamics during *C. elegans* cell fate specification. *Dev. Cell* **42**, 542–553 (2017).

Acknowledgements

We thank S. Grinstein (Hospital for Sick Children, University of Toronto) for stimulating discussions. We thank M. Kozlov (Tel Aviv University) for helping us with the resident charge calculation. We thank D. Andrew, C.-H. Huang, all of the members of the Devreotes and Iglesias laboratories as well as the members of the D. Robinson and M. Iijima laboratories (School of Medicine, Johns Hopkins University) for their valuable suggestions. We thank Y. Long and Y. Deng (Devreotes laboratory) for helping with some experiments. We thank N. Gautam (Washington University School of Medicine in St. Louis) and R. R. Kay (MRC LMB) for providing cells. We thank G. Du (McGovern Medical School, UTHHealth) and A. Müller-Taubenberger (LMU Munich) for sharing plasmids. We thank Addgene and dictyBase for providing the plasmids and resources. This work was supported by NIH grant nos R35 GM118177 (to P.N.D.), DARPA HRO011-16-C-0139 (to P.A.I. and P.N.D.) and AFOSR MURI FA95501610052 (to P.N.D.) as well as NIH grant S10 ODO16374 (to S. Kuo of the JHU Microscope Facility).

Author contributions

T.B. and P.N.D. conceptualized the overall study. T.B. designed and performed all *Dictyostelium* experiments. D.S.P. introduced and developed the mammalian cell culture model and T.B. and D.S.P. together designed and carried out the mammalian experiments. Y.M. provided resources and contributed to the experiments. D.B. and P.A.I. developed the software to compute the CP index and performed localization analyses. T.B. quantified and analysed other results, with input from the other authors. D.B. and P.A.I. developed the computational models and D.B. conducted all of the simulations. T.B., P.N.D., D.S.P., D.B. and P.A.I. wrote the manuscript. P.N.D. and P.A.I. supervised the study.

Competing interests

The authors declare no competing interests.

Additional information

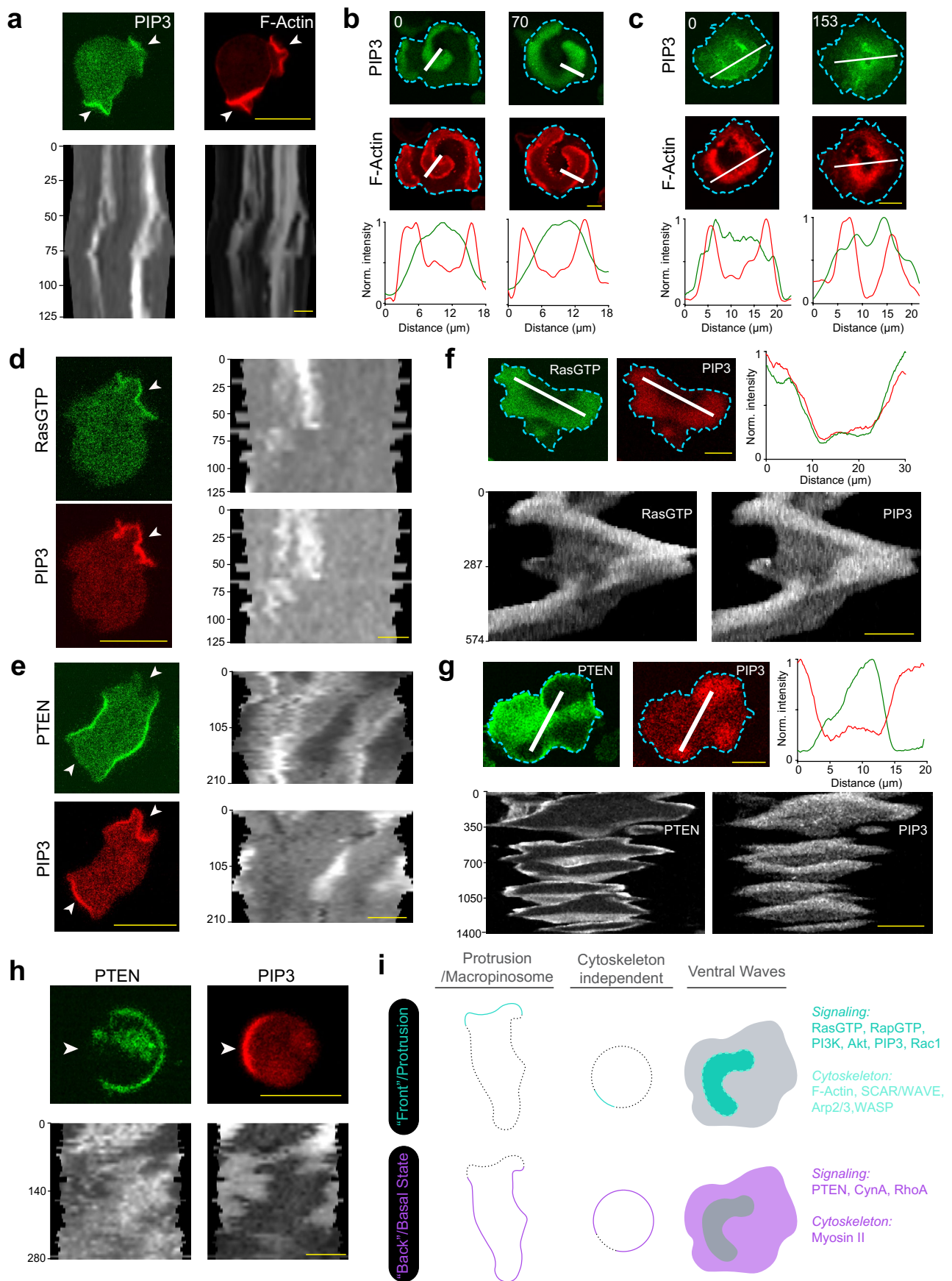
Extended data is available for this paper at <https://doi.org/10.1038/s41556-022-00997-7>.

Supplementary information The online version contains supplementary material available at <https://doi.org/10.1038/s41556-022-00997-7>.

Correspondence and requests for materials should be addressed to Peter N. Devreotes.

Peer review information *Nature Cell Biology* thanks the anonymous reviewers for their contribution to the peer review of this work.

Reprints and permissions information is available at www.nature.com/reprints.

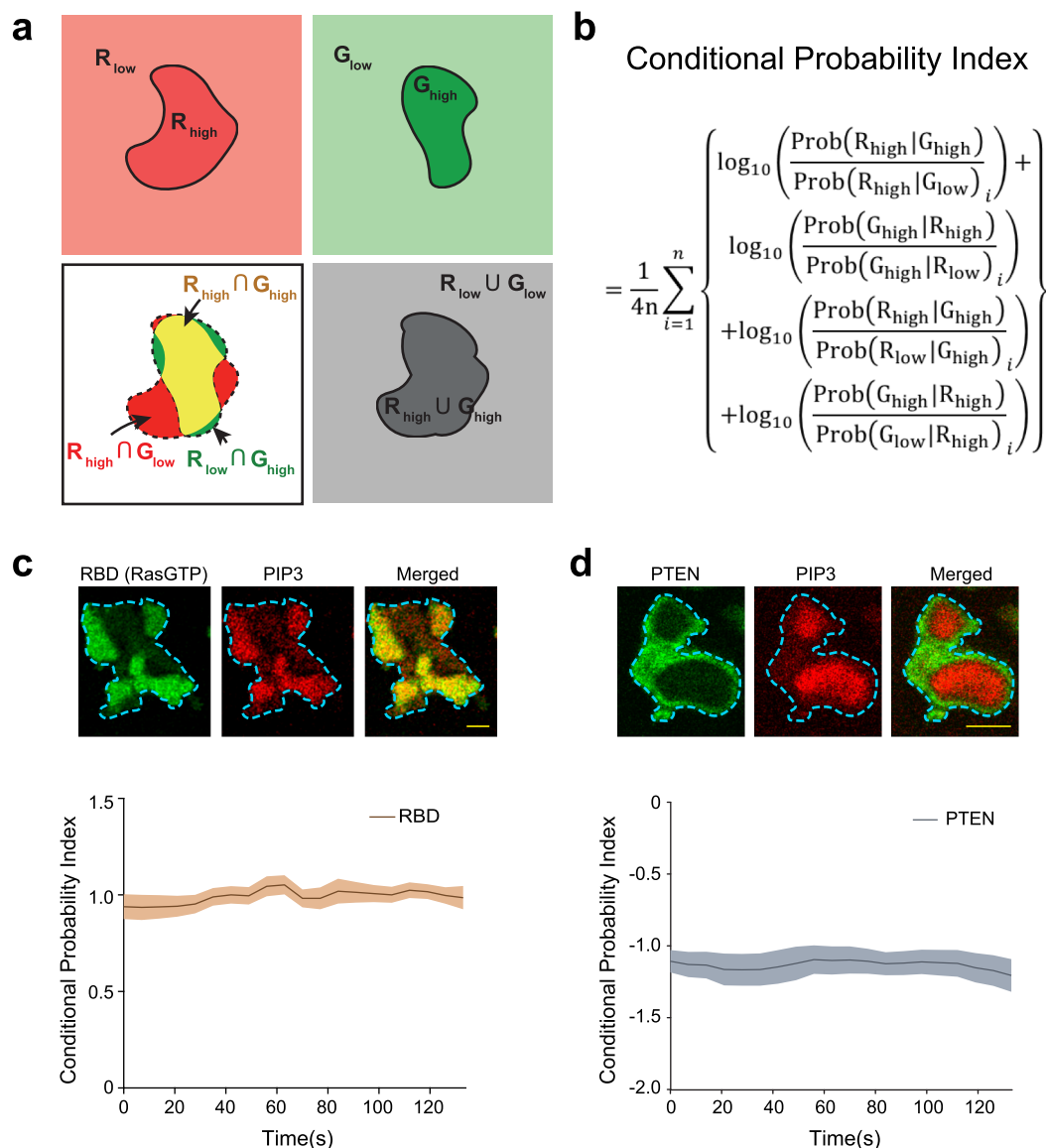


Extended Data Fig. 1 | See next page for caption.

Extended Data Fig. 1 | Cells generate two mutually exclusive dynamic states in the membrane during migration and ventral wave propagation.

(a) Coordinated localization dynamics of signalling (PIP3) and cytoskeletal components (F-actin) in migrating *Dictyostelium* cell protrusions. Top panel: Live-cell images (Arrowheads: Protrusions enriched in both F-actin and PIP3). Bottom panel: 360° membrane kymographs showing consistency of coordination. Here and in all other kymographs, numbers on the left denote time in seconds, unless otherwise mentioned. Throughout this study, PIP3 level is marked by PH_{crac} in *Dictyostelium* and by PH_{AKT} in macrophages, whereas, newly polymerizing F-actin is marked by LimE_{coil} ('LimE' hereafter) in *Dictyostelium* and by Lifeact in macrophages. **(b, c)** Coordinated propagation of signalling (PIP3) and cytoskeletal (F-actin) components in ventral-surface cortical waves of *Dictyostelium* (b) and RAW 264.7 macrophages (c). Top two panels show live-cell images and bottom panels show line-scan intensity profile along the solid white lines. Similar convention is followed throughout this article. **(d, e)** Activated Ras and PIP3 colocalizing in the protrusions (d), whereas PTEN selectively dissociating from it (e), in migrating *Dictyostelium* cells. Left: Live-cell images,

Right: 360° membrane kymographs. Arrowheads: Protrusions/front-states. Throughout this study, Ras-Binding Domain of Raf1 (RBD) was used as a detector of Ras activation. **(f, g)** In propagating waves of *Dictyostelium*, activated Ras and PIP3 dynamically co-localized and defined the front-state regions (f), whereas PIP3 and PTEN exhibit consistent complementarity (g). Live-cell images, line-scan intensity profiles, and line kymographs are shown. **(h)** Complementary distribution of PIP3 and PTEN is independent of cytoskeleton. Here *Dictyostelium* cells are imaged in presence of Latrunculin A (F-actin polymerization inhibitor). Arrowheads denoting front-states. **(i)** Schematic showing the front-back complementary patterning in three different scenarios: migrating cell protrusions, cytoskeleton-independent cortical symmetry breaking, and propagating ventral waves. For first two cases, we could study a 1D profile, whereas for ventral waves, we observed a 2D profile at the substrate-attached surface. Several examples of established signalling and cytoskeletal components are listed and categorized. In all situations, when a front-state was created from the back/basal state of the membrane, back markers moved away from that particular domain, maintaining complementarity. All scale bars are 10 μm.



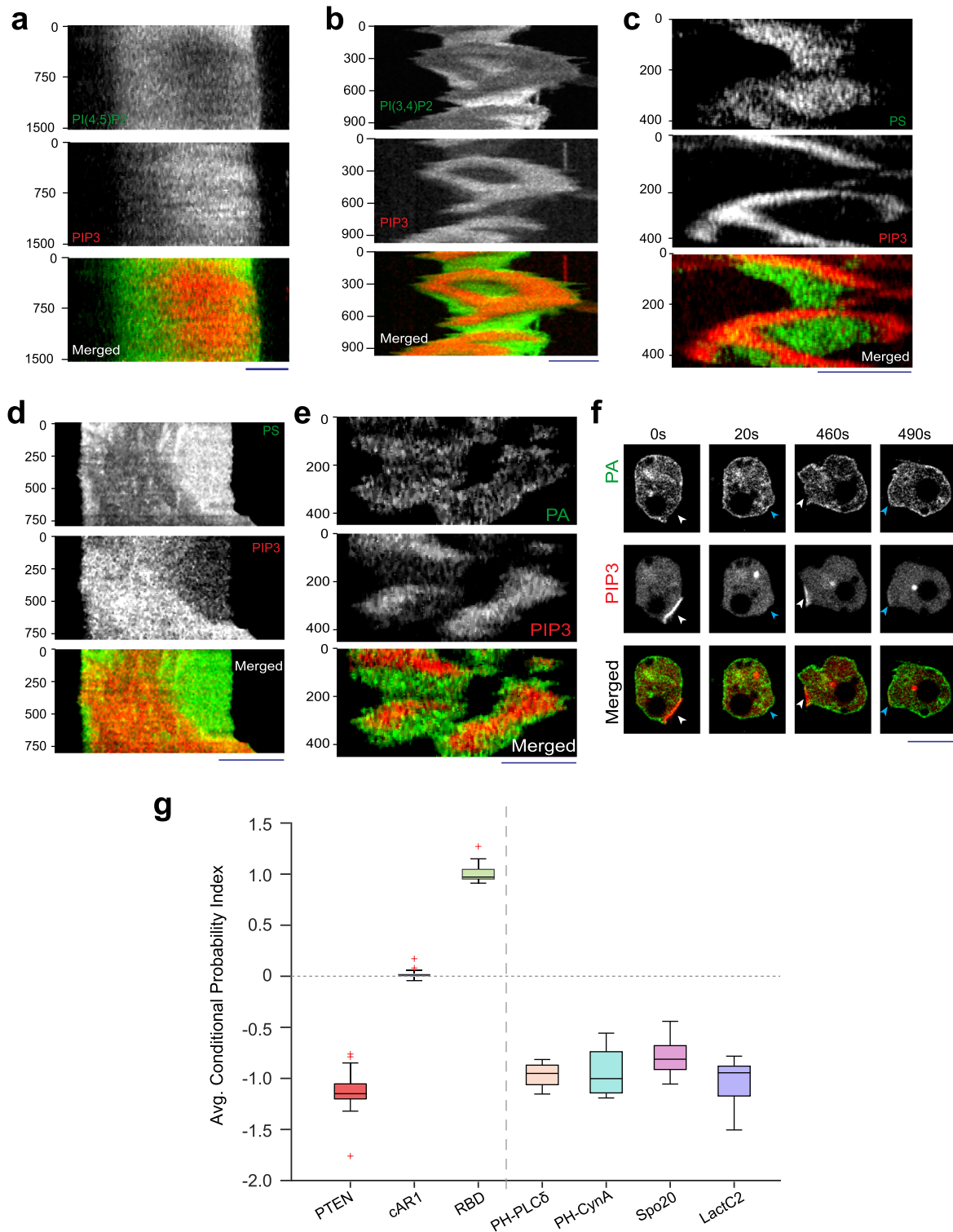
Extended Data Fig. 2 | Developing conditional probability index as a metric to quantify the extent of co-localization and complementary localization. (a)

Schematics showing the application of the concepts of conditional probability in quantifying the degree of co-localization between two entities, R and G.

The regions of the high enrichments of the species R and G are denoted as R_{high} and G_{high} whereas the depleted states are denoted as R_{low} and G_{low} , respectively (top panels). The overlapped region (yellow in the bottom left panel) denotes $R_{\text{high}} \cap G_{\text{high}}$. The other necessary probabilities are also shown which are required in the computation of the respective Conditional Probability Index (CP index).

(b) The mathematical description of the CP index. As usual, $P(R_{\text{high}} | G_{\text{high}})$ denotes Probability of selecting R_{high} , given G_{high} is already selected. Rest of the expression

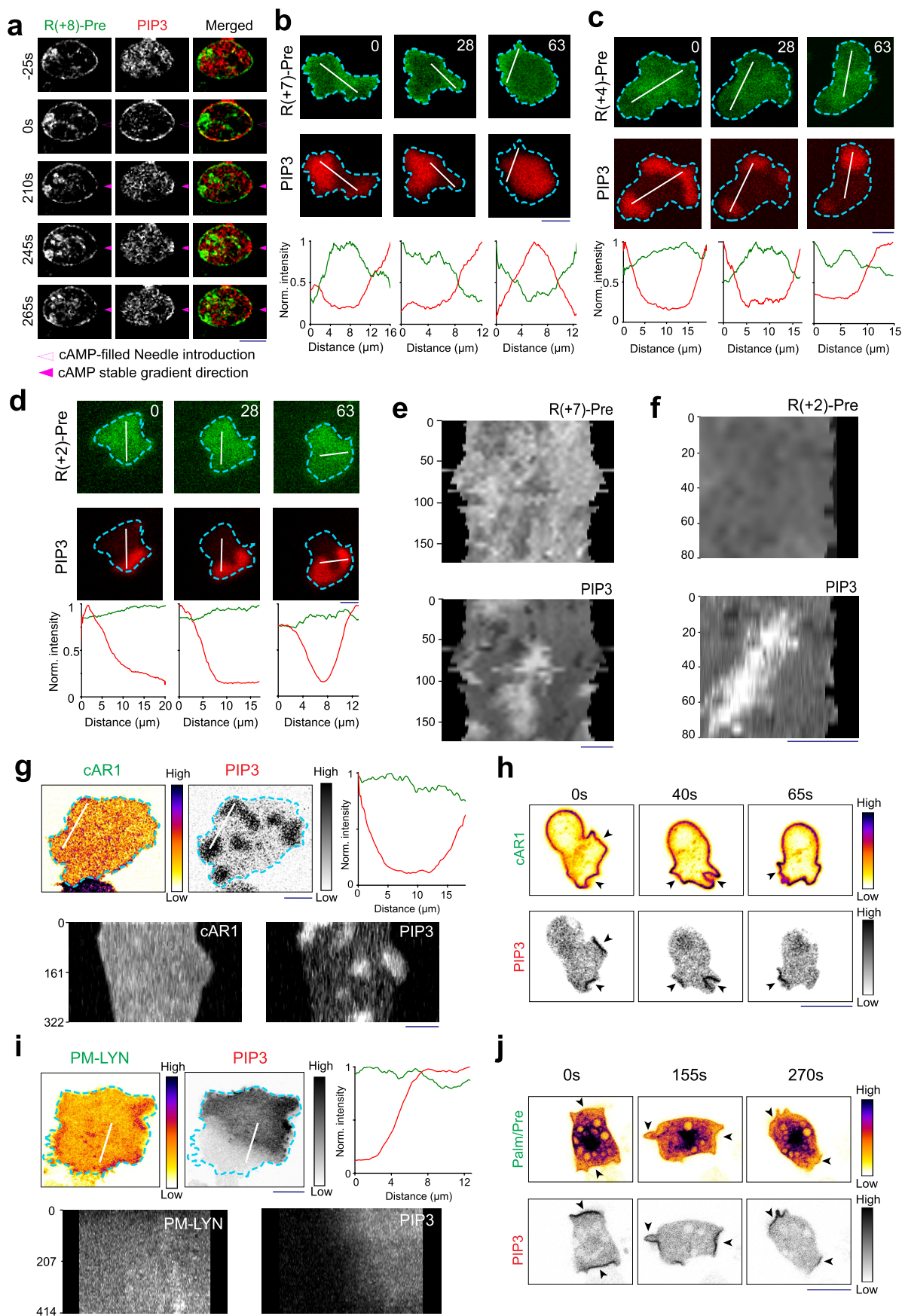
follow the same standard convention (please see methods for details). **(c, d)** Time series plots of CP indices of established back protein PTEN **(c)** and established front sensor RBD **(d)**; number of cells $n_c = 15$ for RBD **(c)** and $n_c = 17$ for PTEN **(d)**. Throughout this paper, to generate CP index time-plots, each cell was analysed for $n_f = 20$ frames; data are mean \pm s.e.m. Top panels show representative images of ventral waves in *Dictyostelium* cells coexpressing either PH_{Crac} and RBD **(c)** or PH_{Crac} and PTEN **(d)**. Note that the CP index value of PTEN is negative and RBD is positive which demonstrate their back-state and front-state localization, respectively. Throughout this paper, all CP indices are calculated with respect to PIP3.



Extended Data Fig. 3 | See next page for caption.

Extended Data Fig. 3 | PI(4,5)P2, PI(3,4)P2, PS, and PA exhibit consistent yet dynamic back-state distribution. (a) Representative line-kymograph of ventral waves in RAW 264.7 macrophages coexpressing PI(4,5)P2 biosensor (GFP- $\text{PH}_{\text{PLC}\beta}$), and PIP3 biosensor (PH_{AKT} -mCherry). Time-lapse images and line-scan intensity profiles were shown in Fig. 1c. (b) Representative line-kymograph of ventral waves in *Dictyostelium* cells coexpressing PI(3,4)P2 biosensor (PH_{CynA} -KikGR) and PIP3 biosensor (PH_{Crac} -mCherry). Time-lapse images and line-scan intensity profiles were shown in Fig. 1d. (c) Representative line kymographs of ventral wave pattern shown in *Dictyostelium* cells coexpressing PS biosensor (GFP-LactC2) and PIP3 biosensor, (PH_{Crac} -mCherry). Time-lapse images and line-scan intensity profiles were shown in Fig. 1g. (d) Representative line kymographs of ventral wave pattern in RAW 264.7 macrophage cells coexpressing PS biosensor (GFP-LactC2) and PIP3 biosensor, (PH_{AKT} -mCherry). Time-lapse images and line-scan intensity profiles were shown in Fig. 1h. (e) Representative

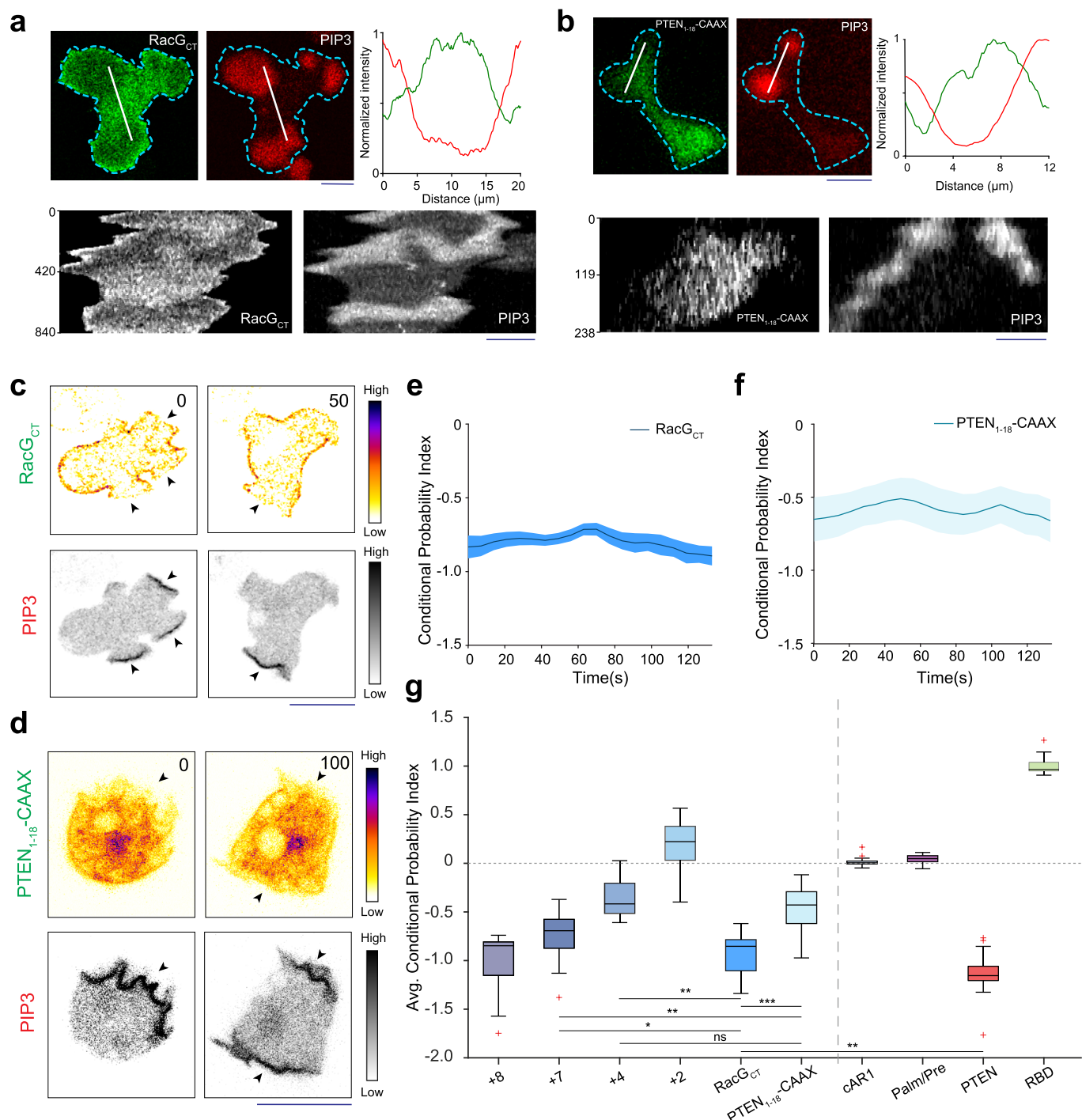
line kymographs of ventral wave pattern in *Dictyostelium* cells coexpressing PA biosensor (GFP-Spo20) and PIP3 biosensor (PH_{Crac} -mCherry). Time-lapse images and line-scan intensity profiles were shown in Fig. 1j. (f) Time-lapse images of migrating *Dictyostelium* cells coexpressing GFP-Spo20 and PH_{Crac} -mCherry. White arrows: Protrusions where PIP3 is enriched and PA is depleted. Blue arrows: Spo20 returned back to the membrane as protrusions were eventually retracted and membrane domain returned to its basal back-state. (g) Box and Whisker plot of time-averaged CP indices of four anionic phospholipids (PI(4,5)P2, PI(3,4)P2, PS, and PA), together with uniform membrane marker control cAR1, back protein PTEN, and front sensor RBD; $n_c = 16$ cells for PI(4,5)P2/ $\text{PH}_{\text{PLC}\beta}$, $n_c = 10$ cells for PI(3,4)P2/ PH_{CynA} , $n_c = 15$ cells for PS/LactC2, $n_c = 16$ cells for PS/Spo20, $n_c = 20$ cells for cAR1, $n_c = 17$ cells for PTEN, $n_c = 15$ cells for RBD. As mentioned earlier, to generate each data point, $n_f = 20$ frames were averaged for the above-mentioned number of cells.



Extended Data Fig. 4 | See next page for caption.

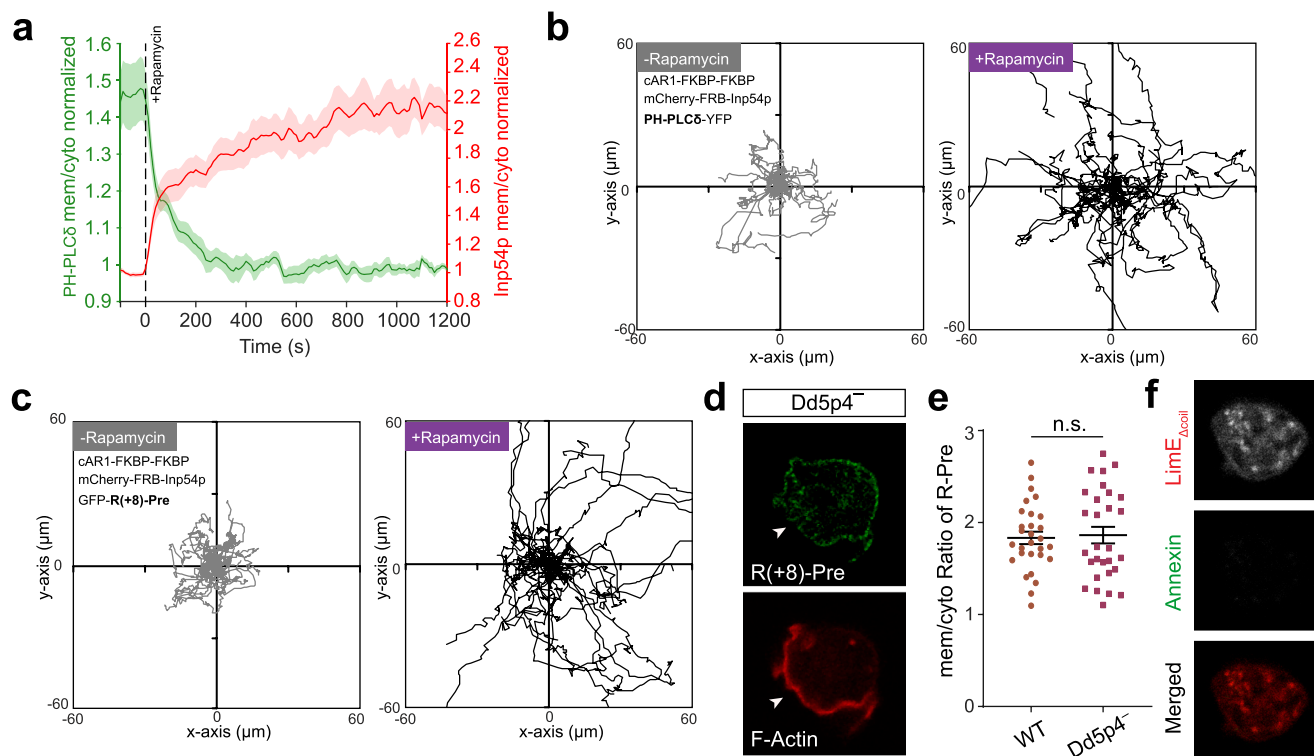
Extended Data Fig. 4 | Spatiotemporal organization of different mutated charge sensors and uniform membrane controls. (a) Representative live-cell images of *Dictyostelium* cells coexpressing GFP-R(+8)-Pre and PH_{crac}-mCherry under chemotactic gradient stimulation. Solid magenta arrowhead indicates the direction of micropipette (filled with 1 μ M cAMP) for gradient stimulation. Dashed magenta arrowhead indicates the introduction of needle (t = 0 s) which is manifested by the transient global response in PH_{crac} channel. Cells were pre-treated with Latrunculin A. (b-d) Live-cell time-lapse images and line scan intensity profiles of *Dictyostelium* cells expressing PH_{crac}-mCherry, along with GFP-R(+7)-Pre (b) or GFP-R(+4)-Pre (c) or GFP-R(+2)-Pre (d), during ventral wave propagation, displaying decreasing extent of back-state preference of the surface charge sensors. The first time points were showed in Fig. 2j (in grayscale colourmap). (e, f) The 360° membrane kymographs of cells shown in Fig. 2k, indicating R(+7)-Pre consistently moves away from PIP3-rich protrusions (e, whereas R(+2)-Pre is uniform over the cortex (f). (g) Live-cell images, line

scan intensity profiles, and representative line kymographs of ventral waves in *Dictyostelium* cells coexpressing PH_{crac}-mCherry and membrane marker cARI-GFP, demonstrating that cARI does not distribute to front- or back- state regions and it is consistently uniform over the membrane. (h) Live-cell time-lapse images of migrating *Dictyostelium* cells coexpressing PH_{crac}-mCherry and cARI-GFP showing cARI is symmetric over the membrane. Black arrows: PIP3-rich protrusions where cARI was present as well. (i) Live-cell images, linescan intensity profiles, and representative line kymographs of ventral waves in RAW 264.7 cells coexpressing PH_{AKT}-mCherry and membrane marker, LYN-GFP, showing consistent uniform profile of LYN over the membrane and no depletion in front-state area. (j) Live-cell time-lapse images of migrating *Dictyostelium* cells coexpressing PH_{crac}-mCherry and GFP-Palm/Pre, showing a symmetric profile of Palm/Pre over the membrane. Black arrows: Protrusions/front-states. In (g-j), the “Fire invert” LUT of Fiji/ImageJ was used so that it can clearly show any small inhomogeneity. For exact sequence details, please see Supplementary Table S1.



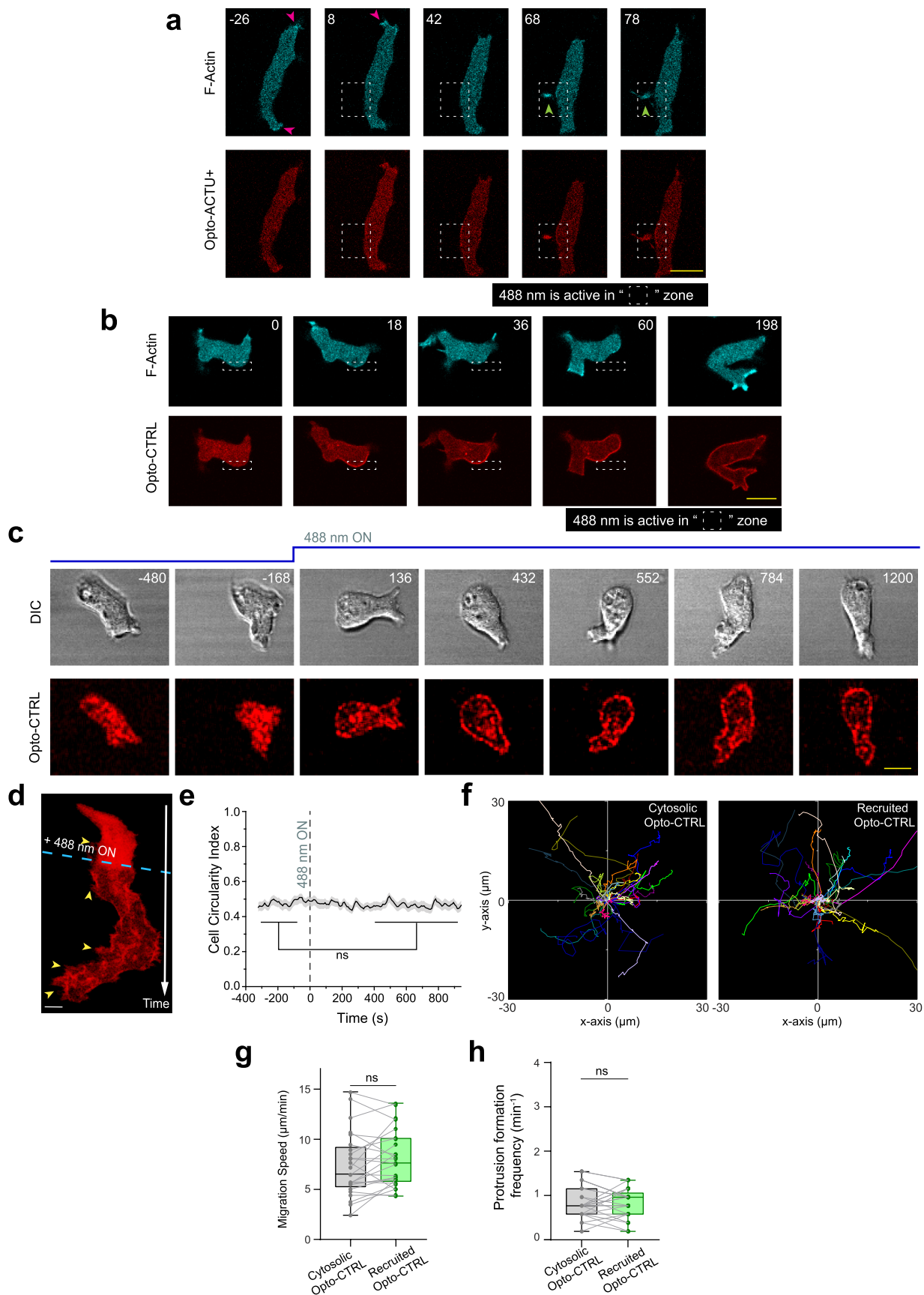
Extended Data Fig. 5 | Different polybasic sequences localize to back-state regions depending on their charge, irrespective of their exact amino-acid sequences. **(a, b)** Representative live-cell images, line scan intensity profiles, and representative line kymographs of *Dictyostelium* cells coexpressing PH_{Crac}-mCherry and GFP-RacG_{CT} (a) or GFP-PTEN₁₋₁₈-CAAX (b), demonstrating consistent dynamic back distribution for RacG_{CT} and limited back distribution for PTEN₁₋₁₈-CAAX in ventral waves. For exact sequence details, please see Supplementary Table S1. **(c, d)** Representative live-cell time-lapse images showing distribution of RacG_{CT} (c) or PTEN₁₋₁₈-CAAX (d) in migrating *Dictyostelium* cells (coexpressing PH_{Crac}-mCherry), demonstrating localization profiles analogous to (a, b). **(e, f)**

f) Time series plots of CPI index of RacG_{CT} (e) and PTEN₁₋₁₈-CAAX (f) show the extent of back localization; $n_c = 17$ for RacG_{CT} (e), $n_c = 12$ for PTEN₁₋₁₈-CAAX (f); mean \pm s.e.m. **(g)** Comparison of localization profile by box plot of time-averaged CPI indices of all surface charge sensors, together with uniform membrane marker controls, back protein PTEN, and front sensor RBD; R(+8)-Pre: $n_c = 30$, R(+7)-Pre: $n_c = 23$, R(+4)-Pre: $n_c = 20$, R(+2)-Pre: $n_c = 12$, RacG_{CT}: $n_c = 17$, PTEN₁₋₁₈-CAAX: $n_c = 12$, cAR1: $n_c = 20$, Palm/Pre: $n_c = 11$, PTEN: $n_c = 17$, RBD: $n_c = 15$. Box and whiskers are graphed as per Tukey's method. All p-values by Mann-Whitney-Wilcoxon test.



Extended Data Fig. 6 | Dynamics of surface charge sensor in PI(4,5)P2 and PI(3,4)P2 depleted cells. (a) Time course of membrane/cytosol ratio of PH_{PLC δ} and Inp54p upon rapamycin addition (indicated by black dashed vertical line), in *Dictyostelium* cells coexpressing cAR1-FKBP-FKBP, mCherry-FBP-Inp54p, and PH_{PLC δ} -GFP, demonstrating PH_{PLC δ} dissociated from membrane upon PI(4,5)P2 depletion; $n = 17$ cells; mean \pm s.e.m. **(b, c)** Cell tracks show the migration profile of *Dictyostelium* cells expressing chemically induced dimerization system cAR1-FKBP-FKBP and mCherry-FBP-Inp54p, along with PH_{PLC δ} -GFP (b) or GFP-R(+8)-Pre (c), before and after rapamycin induced recruitment. Tracks demonstrating similar change in migration profile in both cases, as quantified

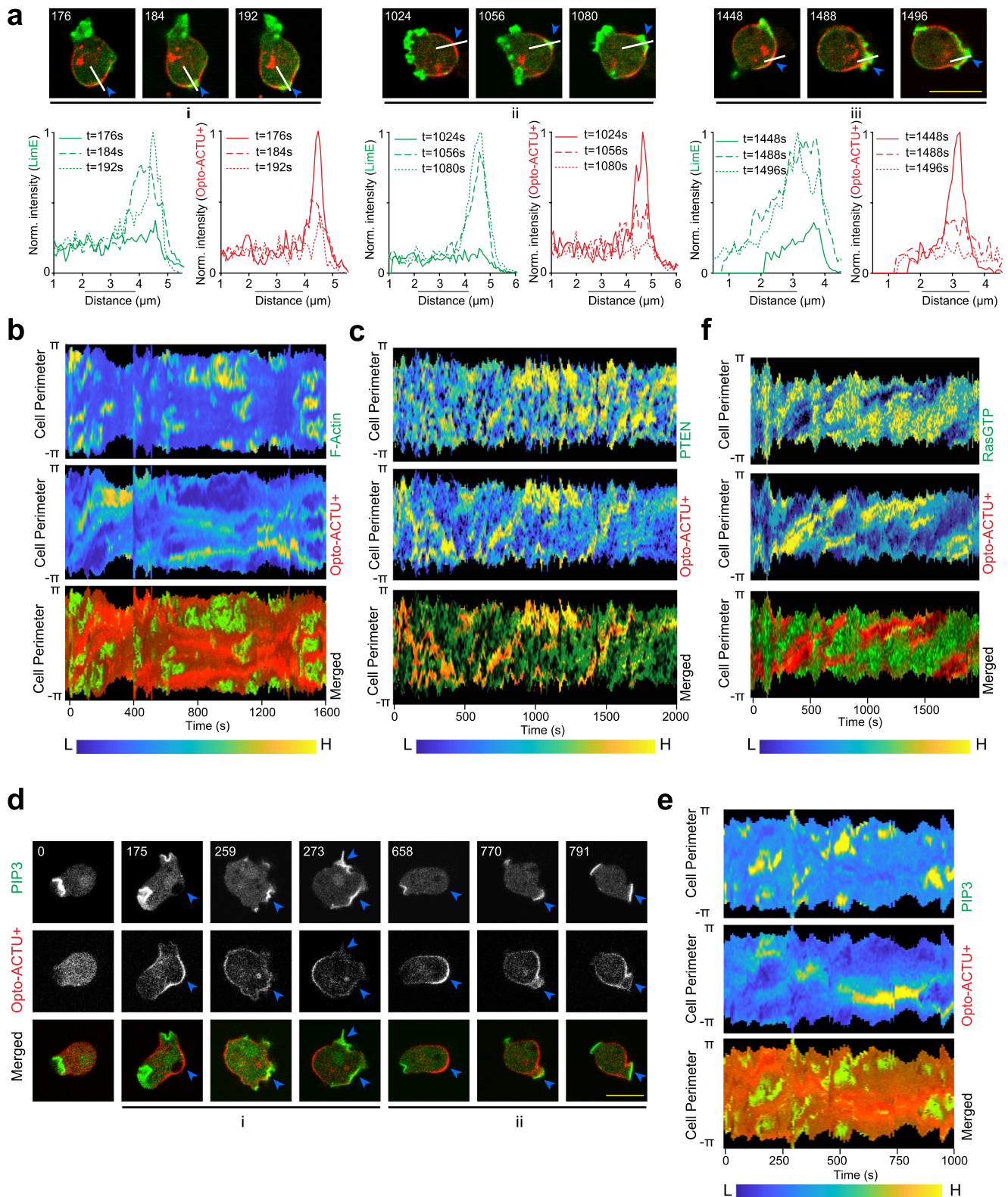
in terms of migration speed in Fig. 3d. To generate each track for $n_c = 32$ cells (in each case), cells were followed for $n_f = 60$ frames (7 s/frame). **(d)** Representative image of Dd5p4 $^{-}$ *Dictyostelium* cell (where PI(3,4)P2 level is low) coexpressing GFP-R(+8)-Pre and LimE-mRFP displaying characteristic membrane association and back localization of R(+8)-Pre; white arrows denote F-actin rich protrusions. **(e)** Quantification of membrane association of R(+8)-Pre in wild type and Dd5p4 $^{-}$ cells, in terms of membrane/cytosol ratio; $n = 29$ cells in each case; p-value by Mann-Whitney-Wilcoxon test. **(f)** Example of a quiet or non-protrusion forming *Dictyostelium* cells expressing LimE-mRFP, whose outer leaflet of membrane was allowed to transiently bind with Annexin V, Alexa Fluor 488 conjugate.



Extended Data Fig. 7 | See next page for caption.

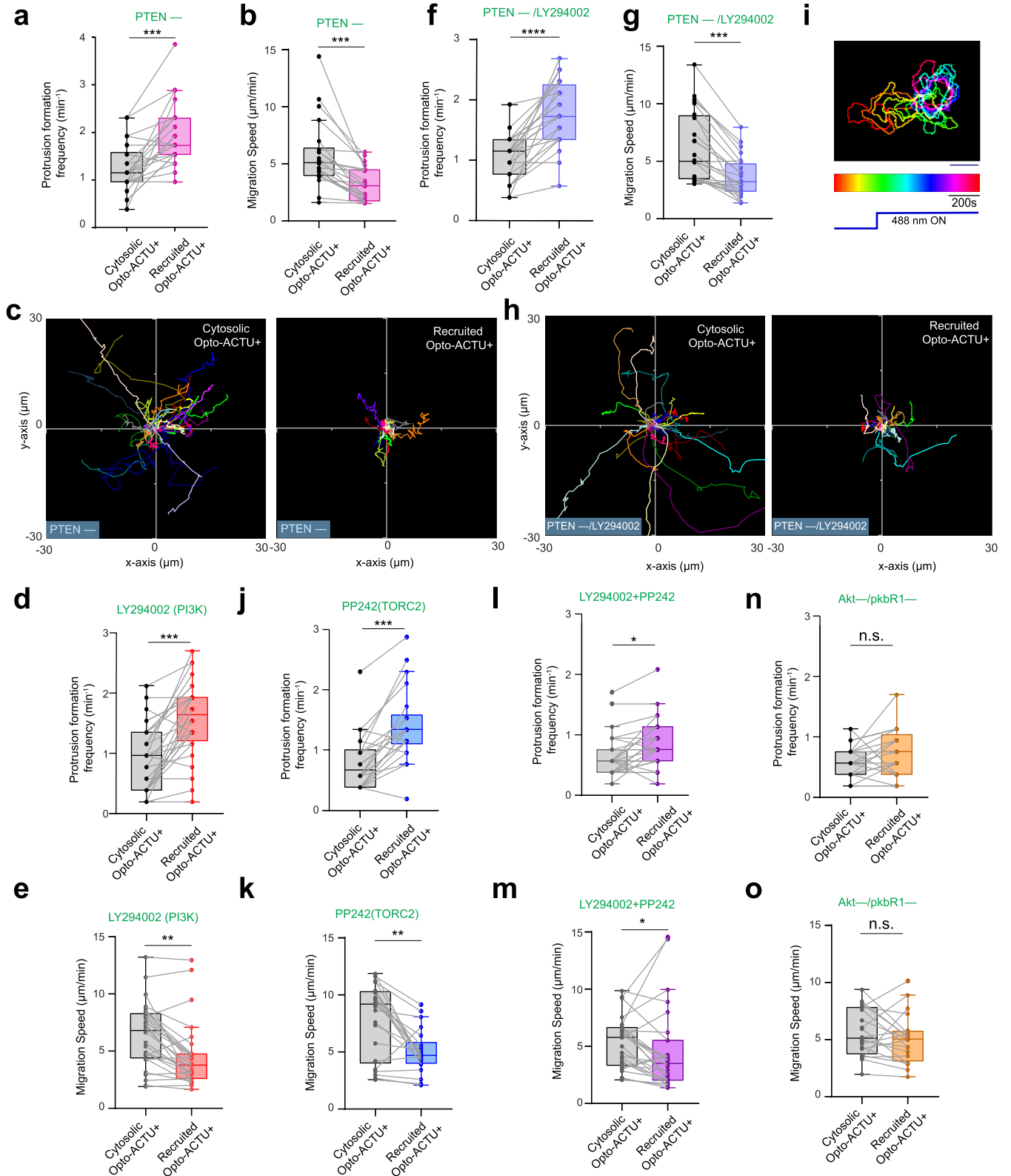
Extended Data Fig. 7 | Local recruitment of Opto-ACTU⁺ in polarized cells induce de novo generation of protrusion near recruitment area, whereas neither local nor global recruitment of uncharged control Opto-CTRL elicit any phenotypic changes. (a) A representative example of *de novo* formation of protrusion from a position of choice in the back-state region of the membrane by spatially confined recruitment of Opto-ACTU⁺. Magenta arrows: Old protrusions, Green arrows: New protrusions. (b) A representative example of spatially confined optogenetic recruitment of Opto-CTRL demonstrating no increase in protrusion generation from the site of recruitment. In (a-b), along with the Opto-ACTU⁺ (a) or Opto-CTRL (b), cells were coexpressing cARI-CIBN and LimE-Halo; the numbers on the images denote time in seconds. (c, d) Time-lapse snapshots (c) and time-stack (d) of *Dictyostelium* cells coexpressing Opto-CTRL and cARI-

CIBN, demonstrating the unaltered cell morphology and migration behaviour in polarized *Dictyostelium* cells, upon optogenetic recruitment. Numbers are time in seconds (c). 488 nm switched ON globally at $t = 0$ s. Yellow arrows: Opto-CTRL is uniform over cortex and did not move away from protrusions (d). (e-h) Quantification of cell morphology and migration mode in terms of cell circularity index (e), cell tracks (f), migration speed (g), and new protrusion formation frequency (h), upon Opto-CTRL recruitment ($n = 25$ cells). Data shown as mean \pm s.e.m. over time in (e). In (f-h), for either before or after recruitment tracks, each cell tracked for $n_f = 40$ frames ($t = 320$ s). Tracks were reset to the same origin in (f). For pairwise comparison, tracks are color-coded in (f) and data from same cell are connected by grey line in (g) and (h). The p-values by Mann-Whitney-Wilcoxon test.



Extended Data Fig. 8 | Global recruitment of Opto-ACTU⁺ can cause spatiotemporally confined activation of Ras/PI3K/AKT/TORC2/F-actin network components. (a) Intensity profiles of LimE-GFP and Opto-ACTU⁺ along the white lines (the images are same as shown in Fig. 6b) demonstrate that F-actin polymerizes in the domains of membrane where Opto-ACTU⁺ accumulates and when that leads to a protrusion, Opto-ACTU⁺ moves away with a short time delay. (b) 360° membrane kymograph of cell shown in Fig. 6b. (c) 360° membrane kymograph of cell shown in Fig. 6c. (d) Time-lapse live-cell images

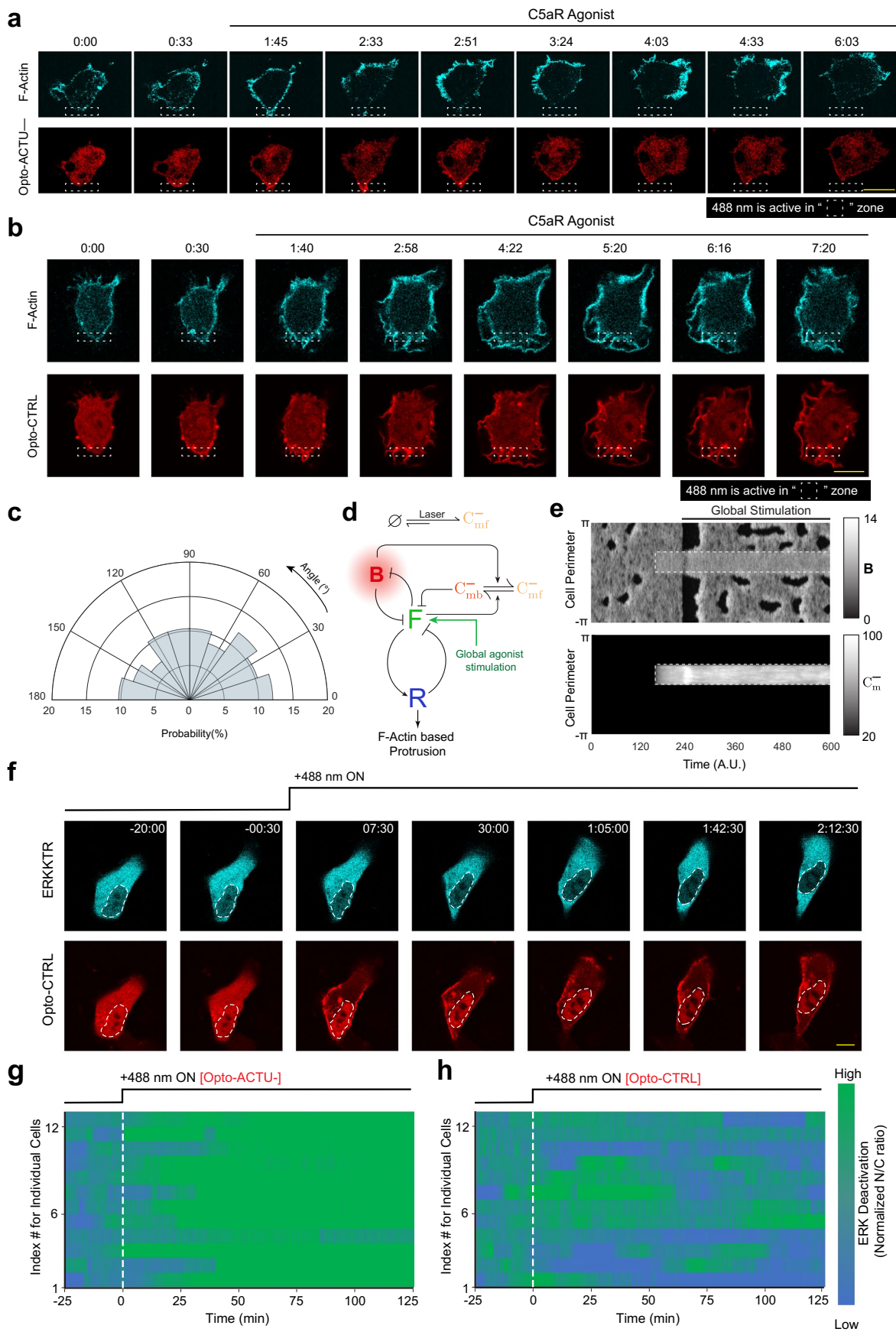
of *Dictyostelium* cells coexpressing Opto-ACTU⁺, cARI-CIBN, and PH_{Crac}-YFP where recruitment was started at $t = 0$ s. Numbers show time in seconds. The “i” and “ii” are showing two different PIP3 production events which eventually lead protrusion formation. For each event, blue arrowheads are showing the areas where Opto-ACTU⁺ was first accumulated which in turn became the areas of PIP3 production and eventually, after protrusion formation, Opto-ACTU⁺ moved away to a newer back-state area. (e) 360° membrane kymograph of cell shown in (d). (f) 360° membrane kymograph of cell shown in Fig. 6d.



Extended Data Fig. 9 | See next page for caption.

Extended Data Fig. 9 | The effect of specific genetic and pharmacological perturbations upon the phenotypic changes induced by Opto-ACTU⁺ recruitment. (a-c) Quantification of migration profile changes in terms of new protrusion formation frequency (a), speed (b), and cell tracks (c), upon Opto-ACTU⁺ recruitment, in *PTEN*-*Dictyostelium* cells; $n_c = 22$ cells. (d, e) Quantification of migration profile changes in terms of new protrusion formation frequency (d) and speed (e), upon Opto-ACTU⁺ recruitment in *Dictyostelium* cells, pre-treated with PI3K inhibitor LY294002; $n_c = 28$ cells. (f-h) Quantification of migration profile changes in terms of new protrusion formation frequency (f), speed (g), and cell tracks (h), upon Opto-ACTU⁺ recruitment in *PTEN*-*Dictyostelium* cells, pre-treated with LY294002; $n_c = 24$ cells. (i) Temporally color-coded cell outlines of a representative migrating *PTEN*-*Dictyostelium* cells, pre-treated with PI3K inhibitor LY294002, showing

cell morphology and migratory profile before and after 488 nm was turned on to recruit Opto-ACTU⁺ (corresponding to Supplementary Video S11). (j-o) Quantification of migration profile changes in terms of new protrusion formation frequency (j, l, n) and migration speed (k, m, o) upon Opto-ACTU⁺ recruitment under different genetic and pharmacological inhibitions. In (j-k) cells were pre-treated with PP242 to inhibit TORC2 ($n_c = 22$ cells); in (l-m) cells were pre-treated with both LY294002 and PP242 to simultaneously block PI3K and PP242 ($n_c = 27$ cells); in (n-o), *AKT*/*PKBRI* double knockout cell line was used ($n_c = 21$ cells). For each case, each of the n_c cells were tracked for $n_f = 40$ frames (8 sec/frame was imaging frequency) and time averages were taken. Tracks were reset to the same origin in (c) and (h). For pairwise comparison, tracks are color-coded in (c) and (h). In all boxplots here, for pairwise comparison, data from same cell are connected by grey lines. The p-values by Mann-Whitney-Wilcoxon test.



Extended Data Fig. 10 | See next page for caption.

Extended Data Fig. 10 | Selective recruitment of uncharged control Opto-CTRL cannot suppress protrusion in RAW 264.7 macrophages or global recruitment of Opto-CTRL cannot deactivate ERK in MCF10A cells, unlike Opto-ACTU⁻. (a) Representative live-cell time-lapse images of RAW 264.7 cells undergoing light-triggered spatially confined recruitment of Opto-ACTU⁻, followed by global stimulation with C5a-receptor agonist, demonstrating selective protrusion suppression in the site where Opto-ACTU⁻ was locally recruited and robust protrusion formation in other areas of cortex. Time in min:sec format. Cells were coexpressing Opto-ACTU⁻, CIBN-CAAX, and Lifeact-mVenus. (b) Representative live-cell time-lapse images of RAW 264.7 cells undergoing light-triggered spatially confined recruitment of Opto-CTRL, followed by global stimulation by C5a-receptor agonist. Time in min:sec format. Cells were coexpressing Opto-CTRL, CIBN-CAAX, and Lifeact-mVenus. (c) Polar histogram indicating probability of protrusion formation is essentially uniform over the cortex upon global stimulation with C5a-receptor agonist, in cells where

Opto-CTRL was recruited locally. $n_c = 12$ cells, $n_p = 59$ protrusions. (d) Schematic showing coupled system of excitable network with Opto-ACTU⁻ input along with global agonist stimulation. (e) The simulated kymographs of B (top) and C_m^- (bottom) in response to local recruitment of Opto-ACTU⁻. The location of recruitment is denoted by the white dashed box. The solid black line denotes the span of global agonist stimulation. (f) Representative live-cell time-lapse images of a MCF10A cell displaying ERK-KTR maintaining its cytosolic distribution upon recruitment of Opto-CTRL to CIBN-CAAX, demonstrating no substantial ERK deactivation; cells were pre-treated with and maintained in a saturated dose of EGF throughout the experiment. Time in hr:min:sec format; 488 nm laser was first turned ON at $t = 0$ min. (g, h) Individual cell level changes in the nuclear/cytosolic ratio of ERK-KTR over time, upon recruitment of Opto-ACTU⁻ (g) or Opto-CTRL (h). Population average is in Fig. 8i. The color scale shown in right is applicable to both panels.

Reporting Summary

Nature Portfolio wishes to improve the reproducibility of the work that we publish. This form provides structure for consistency and transparency in reporting. For further information on Nature Portfolio policies, see our [Editorial Policies](#) and the [Editorial Policy Checklist](#).

Statistics

For all statistical analyses, confirm that the following items are present in the figure legend, table legend, main text, or Methods section.

- | | |
|-------------------------------------|--|
| n/a | Confirmed |
| <input type="checkbox"/> | <input checked="" type="checkbox"/> The exact sample size (n) for each experimental group/condition, given as a discrete number and unit of measurement |
| <input type="checkbox"/> | <input checked="" type="checkbox"/> A statement on whether measurements were taken from distinct samples or whether the same sample was measured repeatedly |
| <input type="checkbox"/> | <input checked="" type="checkbox"/> The statistical test(s) used AND whether they are one- or two-sided
<i>Only common tests should be described solely by name; describe more complex techniques in the Methods section.</i> |
| <input type="checkbox"/> | <input checked="" type="checkbox"/> A description of all covariates tested |
| <input type="checkbox"/> | <input checked="" type="checkbox"/> A description of any assumptions or corrections, such as tests of normality and adjustment for multiple comparisons |
| <input type="checkbox"/> | <input checked="" type="checkbox"/> A full description of the statistical parameters including central tendency (e.g. means) or other basic estimates (e.g. regression coefficient) AND variation (e.g. standard deviation) or associated estimates of uncertainty (e.g. confidence intervals) |
| <input type="checkbox"/> | <input checked="" type="checkbox"/> For null hypothesis testing, the test statistic (e.g. F , t , r) with confidence intervals, effect sizes, degrees of freedom and P value noted
<i>Give P values as exact values whenever suitable.</i> |
| <input checked="" type="checkbox"/> | <input type="checkbox"/> For Bayesian analysis, information on the choice of priors and Markov chain Monte Carlo settings |
| <input checked="" type="checkbox"/> | <input type="checkbox"/> For hierarchical and complex designs, identification of the appropriate level for tests and full reporting of outcomes |
| <input type="checkbox"/> | <input checked="" type="checkbox"/> Estimates of effect sizes (e.g. Cohen's d , Pearson's r), indicating how they were calculated |

Our web collection on [statistics for biologists](#) contains articles on many of the points above.

Software and code

Policy information about [availability of computer code](#)

Data collection

Data analysis https://github.com/tatsatb/Simulation-of-Membrane-Surface-Charge-Perturbation. MATLAB, GraphPad Prism, and OriginPro were used for statistical analysis. Versions: MATLAB 2019a, SDE toolbox 1.4.1, Microsoft Excel 2016, Fiji/ImageJ 1.52i, OriginPro 9.0, Graphpad Prism 8."/>

For manuscripts utilizing custom algorithms or software that are central to the research but not yet described in published literature, software must be made available to editors and reviewers. We strongly encourage code deposition in a community repository (e.g. GitHub). See the Nature Portfolio [guidelines for submitting code & software](#) for further information.

Data

Policy information about [availability of data](#)

All manuscripts must include a [data availability statement](#). This statement should provide the following information, where applicable:

- Accession codes, unique identifiers, or web links for publicly available datasets
- A description of any restrictions on data availability
- For clinical datasets or third party data, please ensure that the statement adheres to our [policy](#)

All data needed to evaluate the conclusions in the paper are present in the main text or the supplementary materials. Numerical source data have been provided in "Source Data" section. Any additional requests for information will be fulfilled by the corresponding author upon reasonable request.

Human research participants

Policy information about [studies involving human research participants and Sex and Gender in Research](#).

Reporting on sex and gender	Not Applicable.
Population characteristics	Not Applicable.
Recruitment	Not Applicable.
Ethics oversight	Not Applicable.

Note that full information on the approval of the study protocol must also be provided in the manuscript.

Field-specific reporting

Please select the one below that is the best fit for your research. If you are not sure, read the appropriate sections before making your selection.

Life sciences Behavioural & social sciences Ecological, evolutionary & environmental sciences

For a reference copy of the document with all sections, see nature.com/documents/nr-reporting-summary-flat.pdf

Life sciences study design

All studies must disclose on these points even when the disclosure is negative.

Sample size	Sample sizes were chosen large enough to account for the heterogeneity among cells. The sample sizes that were used in this paper was based on extensive experience with similar experiments in our laboratory (Miao Y et al. 2017, Lampert T J et al., 2017, Li X et al. 2018, Miao Y et al. 2019, Zhan H et al. 2020, etc). Chosen sample sizes are consistent with those that were reported by other researchers in the field as well (Yang Y et al. 2017, Shellard A. et al. 2018, O'Neill P R et al. 2018, Matsuoka S et al. 2018, Graziano B R et al. 2019, Bisaria A et al. 2020, etc). Similar sample sizes were used for experiment and control group. To generate any data point, usually at least 200 images were analyzed.
Data exclusions	For chemically induced dimerization and optogenetics experiments, for either control or experiment group, data were excluded when there is no recruitment as it essentially implies the absence of expression of the untagged membrane anchor in that particular cell. No other data were excluded from the study.
Replication	All reported findings were reliably reproduced using at least three independent biological replicates.
Randomization	This study does not involve any human or animal subjects. To generate any experiment or control group cell lines, cells were collected randomly from the parental cell lines in culture. Time of performing any drug treatment and/or imaging experiment with any custom cell line was chosen randomly as well.
Blinding	It was not feasible during data collection as differences between experimental and control groups were apparent in most cases. It was not relevant during data analysis as most quantifications were performed by automated image analysis in MATLAB and/or Fiji/ImageJ.

Reporting for specific materials, systems and methods

We require information from authors about some types of materials, experimental systems and methods used in many studies. Here, indicate whether each material, system or method listed is relevant to your study. If you are not sure if a list item applies to your research, read the appropriate section before selecting a response.

Materials & experimental systems

n/a	Involvement
<input type="checkbox"/>	<input checked="" type="checkbox"/> Antibodies
<input type="checkbox"/>	<input checked="" type="checkbox"/> Eukaryotic cell lines
<input checked="" type="checkbox"/>	<input type="checkbox"/> Palaeontology and archaeology
<input checked="" type="checkbox"/>	<input type="checkbox"/> Animals and other organisms
<input checked="" type="checkbox"/>	<input type="checkbox"/> Clinical data
<input checked="" type="checkbox"/>	<input type="checkbox"/> Dual use research of concern

Methods

n/a	Involvement
<input checked="" type="checkbox"/>	<input type="checkbox"/> ChIP-seq
<input checked="" type="checkbox"/>	<input type="checkbox"/> Flow cytometry
<input checked="" type="checkbox"/>	<input type="checkbox"/> MRI-based neuroimaging

Antibodies

Antibodies used	Anti-Bovine Serum Albumin antibody (clone BSA-33), Mouse monoclonal (Sigma-Aldrich; SAB4200688)
Validation	<p>The antibody used in this study has been validated by manufacturer. The validation statement is available in "Product Information" document on Sigma-Aldrich website. The relevant part is quoted here:</p> <p>"Anti-Bovine Serum Albumin (BSA) antibody, Mouse monoclonal (mouse IgG2a isotype) is derived from the BSA-33 hybridoma produced by the fusion of mouse myeloma cells and splenocytes from mouse BALB/c mice immunized with Bovine Serum Albumin (BSA). The isotype is determined by ELISA using Mouse Monoclonal Antibody Isotyping Reagents, Product Number ISO2. The antibody is purified from culture supernatant of hybridoma cells.</p> <p>Anti-Bovine Serum Albumin (BSA) antibody, Mouse monoclonal is specific for bovine serum albumin and is highly reactive with goat and sheep serum albumins. The product is less reactive with dog, turkey and horse serum albumins. Monoclonal Anti-BSA does not cross-react with human, rabbit, guinea pig, chicken, hamster, pig, mouse, cat, pigeon, rat or donkey serum albumins. The antibody may be used in various immunochemical techniques including Immunoblotting (~70kDa), Immunoprecipitation and Indirect ELISA. Detection of the BSA band by Immunoblotting is specifically inhibited."</p>

Eukaryotic cell lines

Policy information about [cell lines and Sex and Gender in Research](#)

Cell line source(s)	RAW 264.7: Gift from N. Gautam, Washington University School of Medicine, St. Louis; it was originally obtained from the Washington University Tissue Culture Support Center and American Type Culture Collection (ATCC, TIB-71). Dictyostelium AX2: Lab stock (originally gift from R.R. Kay, MRC LMB, Cambridge, UK). MCF 10A: Gift from M. Iijima, Johns Hopkins University School of Medicine; it was originally obtained from ATCC (CRL-10317) .
Authentication	Cell lines were originally authenticated by the supplier. All cell lines exhibited expected morphology and growth rate.
Mycoplasma contamination	No mycoplasma contamination was detected.
Commonly misidentified lines (See ICLAC register)	No cell lines used in this study are listed in ICLAC register.